



**Instrumentation and Software for the
VERITAS Project and the Detection
of TeV Gamma-Ray Emission from
the BL Lacertae Object 1ES1959+650**

Conor Dowdall

For the award of M. Sc.
Galway-Mayo Institute of Technology

Supervisor: Dr. Patrick Moriarty
Co-supervisor: Prof. David J. Fegan

Submitted to the Higher Education and Training
Awards Council, February 2003.



GMIT

GALWAY-MAYO INSTITUTE OF TECHNOLOGY
INSTITIÚD TEICNEOLAÍOCHTA NA GAILLIMHE-MAIGH EÓ

POSTGRADUATE RESEARCH THESIS

DECLARATION

I, Conor Dowdall, hereby declare that the research described in this dissertation, presented for the award of the degree of Master of Science, was carried out by me at the Galway-Mayo Institute of Technology under the supervision of Dr Patrick Moriarty (GMIT) and Professor David J. Fegan (NUI Dublin), and represents exclusively my own work, except where the contributions of others are indicated in the text.

Candidate Conor Dowdall
Conor Dowdall

Date 26/06/'03

Supervisor Patrick Moriarty
Dr. Patrick Moriarty

Supervisor David J. Fegan
Professor David J. Fegan

Instrumentation and Software for the VERITAS Project and the Detection of TeV Gamma-Ray Emission from the BL Lacertae Object 1ES1959+650

Conor Dowdall

Abstract

Transmission of Cherenkov light through the atmosphere is strongly influenced by the optical clarity of the atmosphere and the prevailing weather conditions. The performance of telescopes measuring this light is therefore dependent on atmospheric effects. This thesis presents software and hardware developed to implement a prototype sky monitoring system for use on the proposed next-generation gamma-ray telescope array, VERITAS. The system, consisting of a CCD camera and a far-infrared pyrometer, was successfully installed and tested on the ten metre atmospheric Cherenkov imaging telescope operated by the VERITAS Collaboration at the F.L. Whipple Observatory in Arizona.

The thesis also presents the results of observations of the BL Lacertae object, 1ES1959+650, made with the Whipple ten metre telescope. The observations provide evidence for TeV gamma-ray emission from the BL Lacertae object, 1ES1959+650, at a level of more than 15 standard deviations above background. This represents the first unequivocal detection of this object at TeV energies, making it only the third extragalactic source seen at such levels of significance in this energy range. The flux variability of the source on a number of timescales is also investigated.

Acknowledgements

There are many people whom I would like to thank for their contributions and influences over the last two years. My particular thanks go to my supervisor, Dr. Pat Moriarty, whose understanding and knowledge never ceased to impress me, and whose advice and help made this project something I am proud of. All of the staff at GMIT also deserve my thanks for having made studying and working there a pleasure. I thank the students at UCD, Stephen Gammell, Bevin Power-Mooney, and John Kildea, for their friendship and help during my time with them. I also thank the staff at UCD, my co-supervisor, Prof. Dave Fegan, and Dr. John Quinn, who not only placed the college's facilities at my disposal but were also extremely helpful and always advised me with informed opinions whenever I needed them.

My family deserve my particular gratitude for everything they have given me over the last two years and beyond, so thanks to my mother and father, my sister, Louisa, my brothers, Shane & Kenny, and Shane's wife, Mandy. I also extend my appreciation to all of my friends from Dublin, everyone I met in Galway and everyone I know whose influence has helped to make me the person I am today.

Final thanks go to everyone I met during my three month visit to Arizona. To all the observers, Mary Kertzman, Karl Kosack, Paul Rebillot, Abe Falcone, Martin Schroedter, John Finley, and Rene Ong among others, who somehow managed to help make ten hours of looking at a computer screen seem not quite so bad, I thank you. In particular, I thank Joe Melnick for his friendship during my three month stay and I wish him all the best.

My sincerest thanks to you all.

“It is a sad thing to think of, but there is no doubt that Genius lasts longer than Beauty. That accounts for the fact that we all take such pains to over-educate ourselves.”

Lord Henry Wotton from *The Picture of Dorian Gray*

- Oscar Wilde.

Contents

1	Gamma-Ray Astronomy and the Imaging Atmospheric Cherenkov Technique	1
1.1	Introduction	1
1.2	Production of Cosmic Gamma Radiation	3
1.3	Detection of Cosmic Gamma Radiation Using the Imaging At- mospheric Cherenkov Technique	7
1.4	The Whipple Observatory Gamma-Ray Telescope	11
1.5	The VERITAS Project	14
1.6	Sky Monitoring Instrumentation for VERITAS	18
2	Prototype Instrumentation for the VERITAS Project	19
2.1	Introduction	19
2.2	The CCD Camera	20
2.2.1	Principle of Operation of the CCD	20
2.3	Installation of the SBIG ST-237 CCD Camera	23
2.4	CCD Camera Results	29
2.5	The FIR Pyrometer	32
2.5.1	Infrared Pyrometry	35
2.5.2	Emissivity	36
2.5.3	The Heitronics KT15D Series Pyrometers	36
2.5.4	FIR Pyrometer Results	39
3	Prototype Software for the VERITAS Project	46
3.1	Introduction	46

3.2	XML Over TCP/IP	47
3.2.1	Client/Server Communications	47
3.3	The Qt GUI Application Framework	49
3.4	The CCD Camera Software	56
3.4.1	Image Processing for the CCD Camera	58
3.5	The FIR Pyrometer Software	65
4	Analysis of TeV Images from the Whipple 10m Reflector	68
4.1	Observing Modes	68
4.2	Image Prefiltering and Parameterisation	69
4.3	The Atmospheric Cherenkov Imaging Technique	71
4.3.1	Hillas Parameters	73
4.3.2	Rate and Significance	75
5	Detection of TeV Gamma-Ray Emission from the BL Lacertae Object 1ES1959+650	81
5.1	Introduction	81
5.2	Motivation for Observations on 1ES1959+650	85
5.3	TeV Emission from 1ES1959+650	86
5.4	Variability Analysis	88
6	Conclusions and Future Work	93
6.1	The CCD Camera and FIR Pyrometer	93
6.2	Active Galactic Nuclei at TeV Energies	95
6.3	The Future of Gamma-Ray Astronomy	96
A	Definition of the Hillas Parameters	98

List of Figures

1.1	The blackbody radiation spectrum.	3
1.2	An illustration of bremsstrahlung or braking radiation, where radiation is emitted as an electron decelerates in the vicinity of a nucleus.	4
1.3	An illustration of synchrotron emission, where photons are emitted at tangents to the path of an electron spiralling around a magnetic field line.	6
1.4	Part of an electromagnetic air shower, which produces a cascade of electrons, positrons, and further gamma rays.	8
1.5	A gamma-ray induced electromagnetic air shower producing Cherenkov radiation, detected by an atmospheric Cherenkov radiation detector.	10
1.6	The current Whipple ten metre telescope in its stowed position.	12
1.7	The Whipple ten metre telescope GRANITE III, 490-pixel camera. Note the inner camera, comprising 379 13mm PMTs, and the three outer rings of 28mm PMTs.	13
1.8	The proposed layout of the seven VERITAS telescopes.	15
1.9	An engineering sketch of a VERITAS telescope.	16
1.10	The flux sensitivities of various gamma-ray detectors.	17
2.1	A CCD chip reading out an image from its array of electrodes. The values are transferred vertically one line at a time and then transported serially via the readout register to the on-chip amplifier.	22

2.2	Two views of the CCD camera and FIR pyrometer in their protective housing (with the top cover removed for purpose of photograph).	24
2.3	The CCD camera FOV (represented by the rectangle) and a VERITAS telescope FOV (represented by the circle).	24
2.4	The CCD camera/FIR pyrometer housing in its original position (arrowed) on the side arm of the Whipple ten metre telescope.	26
2.5	The CCD camera/FIR pyrometer housing box mounted on the bottom arm of the Whipple ten metre telescope (left view and front view; arrowed).	26
2.6	A diagram of the CCD camera connected to its CPU, which in turn is connected to a computer.	27
2.7	A diagram of the CCD camera in its housing, connected to the mount computer in two stages.	28
2.8	The focused CCD camera mounted in its housing on one of the side arms of the Whipple ten metre telescope. The housing cover was removed for the purpose of illustration.	30
2.9	Calculation of the CCD's field of view.	30
2.10	A ten second CCD exposure using an $f/0.85$ lens on the star field in the direction of 1ES1959+650 (RA = 19h 59m, Dec. = 65°00').	31
2.11	A star chart generated using <i>KStars</i> software for the star field in the direction of 1ES1959+650 (RA = 19h 59m, Dec. = 65°00').	32
2.12	A ten second CCD exposure using an $f/0.85$ lens on the star field in the direction of the Crab Nebula (RA = 5h 31m 34.4s, Dec. = 21°58'40.2"). The numbers in brackets are the stellar magnitudes. A star chart for the same field is shown in Figure 2.13.	33

2.13	A star chart generated using <i>KStars</i> software for the star field in the direction of the Crab Nebula (RA = 5h 31m 34.4s, Dec. = 21°58'40.2"). The numbers in brackets are stellar magnitudes. The field shown is approximately the same as that in Figure 2.12. The solid line which runs across the field is the ecliptic.	34
2.14	The Heitronics model KT15D infrared pyrometer.	38
2.15	The RS232 standard interface pin out.	38
2.16	The pins used in the RS232 interface to control to FIR pyrometer.	40
2.17	Graph of temperature read from FIR pyrometer versus emissivity setting for varying ambient temperature settings.	40
2.18	Plot of FIR pyrometer temperature readings while pointing to zenith at the ten metre telescope on the morning of September 12th, 2002.	41
2.19	Raw cosmic-ray data rate recorded with the Whipple ten metre telescope while pointing at NGC4736 from UT 05:11 to 05:41 on June 12th, 2002.	42
2.20	FIR pyrometer temperature readings while pointing at NGC4736 from UT 05:11 to 05:41 on June 12th, 2002. The time interval for these data is the same as for data in Figure 2.19.	43
2.21	Raw cosmic-ray data rate from the Whipple ten metre telescope while pointing at 1ES1959+650 from UT 07:43 to 08:11, June 7th, 2002.	44
2.22	FIR pyrometer temperature readings while pointing at 1ES1959+650 from UT 07:43 to 08:11 on June 7th, 2002. The time interval for these data is the same as for data in Figure 2.21	44
2.23	Comparison of FIR pyrometer temperature for two separate runs with similar raw cosmic-ray data rates (~900 events per minute).	45

3.1	A client computer and display, communicating with a server computer, which is connected to a device that reads out data.	48
3.2	The various stages in XML client/server communications.	49
3.3	An illustration of how inheritance is used in Qt widgets.	51
3.4	Example of the code used to create a basic widget using Qt.	51
3.5	A screen-shot of a basic Qt widget with only one pushbutton, entitled "Hello world!".	52
3.6	An excerpt from the header file which defines the appearance of the CCD control panel developed for the CCD GUI used in this project.	53
3.7	A screen-shot of the custom widget, which is used in the CCD client GUI (Figure 3.12).	54
3.8	A screen-shot of the custom widget, which is used in the weather station client GUI.	55
3.9	Illustration of the hierarchy for the weather station GUI class.	56
3.10	An example of the base-64 encoding process	57
3.11	Format of an archived image file.	58
3.12	A screen-shot of the CCD GUI (the star field in the image is in the direction of the active galaxy H1426).	59
3.13	An 8×6 CCD pixel array containing an image of a star. The numbers 00 to 47 identify the individual pixels.	60
3.14	Identifying a star using the island-finding algorithm. The sequence of steps is indicated by the arrows.	61
3.15	A CCD image, taken while pointed at zenith at UT 07:48:53 on June 19th, 2002.	63
3.16	A screen-shot of the CCD GUI after applying the star-finding algorithm to the CCD image in Figure 3.15. Each star found is represented by a dot for its centre of intensity (as calculated by moment analysis) and a circle with radius proportional to the sum of its total pixel intensity.	64

3.17	A plot of log(brightness) vs. star magnitude for stars located by the star-finding algorithm in a CCD image.	65
3.18	A screen-shot of the FIR pyrometer GUI.	66
4.1	A gamma-ray induced image (left) and a hadron-induced image at the focal plane of an imaging Cherenkov telescope (right)	72
4.2	A gamma-ray initiated air shower (left) and a hadron-initiated air shower (right)	73
4.3	A gamma-ray event imaged on an array of PMTs with an ellipse fitted to it to characterise its shape. The size of the circle represents the tube intensity. Red tubes are “picture” tubes and green tubes are “boundary” tubes.	74
4.4	Diagram illustrating the Hillas parameters.	76
4.5	Plot of the <i>Alpha</i> distribution of events passing the shape cuts for <i>on</i> and <i>off</i> data taken in the direction of the Crab Nebula.	78
4.6	Plot of the <i>Alpha</i> distribution for events passing the shape cuts for <i>tracking</i> data taken on Markarian 421 in January 1998.	80
5.1	Ground-based and Hubble Space Telescope images of the active galaxy NGC4261.	82
5.2	The spectral energy distribution of Mrk 421 (top) and Mrk 501 (bottom) from contemporaneous and archival observations (Buckley et al. 1997; Kataoka et al. 1999; Catanese et al. 1997b; Catanese & the Whipple Collaboration 1999). The curves are meant to guide the eye to contemporaneously measured points and do not represent fits to the data	84
5.3	Plot of average daily rates for data taken on 1ES1959+650 in May and June 2002.	87
5.4	<i>Alpha</i> plot for <i>on/off</i> analysis of 1ES1959+650 data (May–June 2002)	89
5.5	<i>Alpha</i> plot for <i>tracking</i> analysis of 1ES1959+650 data (May–June 2002)	89

5.6	A histogram of χ^2 probabilities for observing days during May and June 2002.	91
5.7	A plot of χ^2 probabilities for observing days during May and June 2002.	92

List of Tables

1.1	Approximate wavelengths, frequencies and energies for the main regions of the electromagnetic spectrum.	2
1.2	Gamma-ray energy ranges, observing techniques and platforms.	2
1.3	Imaging atmospheric Cherenkov telescopes currently in operation.	12
2.1	Summary of the main specifications for the KT15D FIR pyrometer.	37
2.2	Pin-outs for RS232 communications.	39
3.1	The magnitudes and brightnesses (determined by summing pixel values for the stars in the CCD image) of the stars used in the plot in Figure 3.17	64
4.1	The standard set of parameter cuts used by the Whipple Collaboration for data taken during the 2001–2002 observing season.	77
4.2	The standard set of parameter cuts used by the Whipple collaboration for data taken in 1997, during the 1996–1997 observing season.	80
5.1	Rates, significances and elevations for first two days of the detection of 1ES1959+650 at the Whipple Observatory.	87

Chapter 1

Gamma-Ray Astronomy and the Imaging Atmospheric Cherenkov Technique

1.1 Introduction

Gamma radiation is the most energetic form of electromagnetic radiation, with individual photon energies greater than 10^5eV , corresponding to wavelengths less than about 0.01nm . In common with other electromagnetic radiation, gamma-ray photon trajectories are not affected by diffuse interstellar magnetic fields and therefore directly indicate the direction to their source, in contrast to the situation with charged cosmic-ray particles. Moreover, unlike radiation at lower energies, gamma radiation is not attenuated significantly within the Galaxy and therefore essentially provides an unobstructed view through the plane of the Galaxy.

Table 1.1 gives approximate wavelengths, frequencies and energies for the main regions of the electromagnetic spectrum. Gamma-ray energies range over 15 decades, from $\sim 10^5\text{eV}$ to as high as 10^{20}eV (see Table 1.2).

From the point of view of astrophysics, the gamma-ray region may be further subdivided as shown in Table 1.2. The table also indicates the detec-

Region	Wavelength/m	Frequency/Hz	Photon Energy eV
Radio	> 0.1	$< 3 \times 10^9$	$< 10^{-5}$
Microwave	$0.1 - 1 \times 10^{-4}$	$3 \times 10^9 - 3 \times 10^{12}$	$10^{-5} - 0.01$
Infrared	$1 \times 10^{-4} - 7 \times 10^{-7}$	$3 \times 10^{12} - 4.3 \times 10^{14}$	$0.01 - 2$
Visible	$7 \times 10^{-7} - 4 \times 10^{-7}$	$4.3 \times 10^{14} - 7.5 \times 10^{14}$	$2 - 3$
Ultraviolet	$4 \times 10^{-7} - 1 \times 10^{-9}$	$7.5 \times 10^{14} - 3 \times 10^{17}$	$3 - 1 \times 10^3$
X-ray	$1 \times 10^{-9} - 1 \times 10^{-11}$	$3 \times 10^{17} - 3 \times 10^{19}$	$1 \times 10^3 - 1 \times 10^5$
Gamma-ray	$< 10^{-11}$	$> 3 \times 10^{19}$	$> 10^5$

Table 1.1: Approximate wavelengths, frequencies and energies for the main regions of the electromagnetic spectrum.

tion techniques and observing platforms relevant to the different subdivisions (Weekes 1988). Of particular importance for the present work is the very high energy (VHE) region, ranging from about 10GeV to 100TeV.

Energy/eV	Classification	Technique	Observing Platform
$5.1 \times 10^5 - 1 \times 10^7$	Low	NaI Crystal	Satellite
$1 \times 10^7 - 3 \times 10^7$	Medium	Compton Telescope	Satellite
$3 \times 10^7 - 1 \times 10^{10}$	High	Spark Chamber	Satellite
$1 \times 10^{10} - 1 \times 10^{14}$	Very High	Atmospheric Cherenkov	Ground Level (Mountain)
$1 \times 10^{14} - 1 \times 10^{17}$	Ultra High	Air Shower Array	Ground Level (Mountain)
$1 \times 10^{17} - 1 \times 10^{20}$	Extremely High	Air Shower Array	Ground Level (Sea Level)

Table 1.2: Gamma-ray energy ranges, observing techniques and platforms.

1.2 Production of Cosmic Gamma Radiation

Many astrophysical systems emit radiation which is essentially thermal in origin. However, thermal processes cannot account for cosmic gamma radiation, particularly at energies in the VHE region and above. To see this, consider the spectrum of radiation emitted by a blackbody radiator. The blackbody radiation spectrum is given by Planck's law:

$$B(\nu, T) = \frac{8\pi\nu^2}{c^3} \frac{h\nu}{e^{h\nu/kT} - 1}, \quad (1.1)$$

where $B(\nu, T)$ is the energy density at frequency ν , for a blackbody at temperature T , and c is the speed of light. Figure 1.1 shows the shape of the spectrum for different temperatures. If λ_m represents the wavelength at

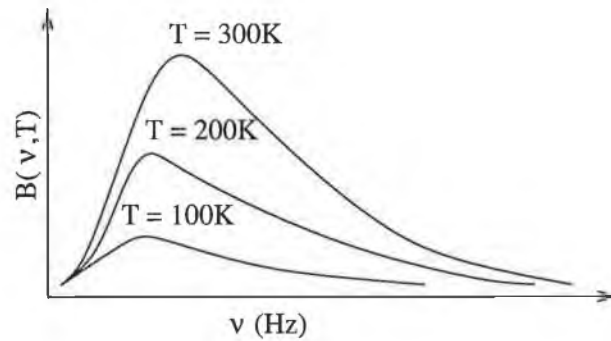


Figure 1.1: The blackbody radiation spectrum.

which the blackbody spectrum peaks for a given temperature T , the product $\lambda_m T$ is constant (Wien's displacement law):

$$\lambda_m T = 2.898 \times 10^{-3} \text{m.K} = a, \text{ constant.} \quad (1.2)$$

Since photon energy is equal to Planck's constant times speed of light divided by wavelength, the photon energy E_m , corresponding to the peak of the spectral brightness distribution, is proportional to the temperature T , as shown in Equation 1.3.

$$E_m = \frac{hc}{\lambda_m} = \frac{hcT}{a} \propto T. \quad (1.3)$$

Most of the photons emitted by a hot body have wavelengths of the order of λ_m and energies of the order of E_m . However, even for temperatures as high as 10^6K , E_m is less than 1keV , so it is clear that thermal processes cannot account for the production of VHE gamma radiation with photon energies exceeding 10^7keV . We must therefore look to non-thermal processes for the origin of such radiation.

Non-thermal processes which give rise to electromagnetic radiation include radioactive decay of nuclei or particles, collisions involving high-energy particles, particle-antiparticle annihilation and acceleration of charged particles. For example, high-energy electrons can emit gamma radiation as a result of electromagnetic interaction with nuclei (bremsstrahlung), photons (inverse Compton scattering) or magnetic fields (synchrotron radiation). Each of these processes is described in more detail below.

Bremsstrahlung

Bremsstrahlung, or braking radiation, describes the radiation emitted when a charged particle is decelerated, for example, in the electric field of a nucleus. Figure 1.2 illustrates the process.

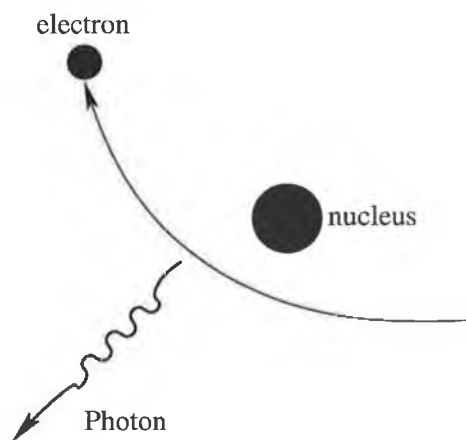


Figure 1.2: An illustration of bremsstrahlung or braking radiation, where radiation is emitted as an electron decelerates in the vicinity of a nucleus.

Inverse Compton Scattering

The Compton effect is the scattering of a photon interacting with a charged particle, for example, an electron. Energy is transferred to the electron from the photon, which therefore emerges from the interaction with a longer wavelength. If the scattered radiation emerges at an angle ϕ with respect to the incident direction, and if λ and λ' are the wavelengths of the incident and scattered radiation respectively, then

$$\lambda' - \lambda = \frac{h}{mc}(1 - \cos \phi),$$

where m is the electron rest mass, h is Planck's constant and c is the speed of light.

In *inverse* Compton scattering a photon *gains* energy by interacting with a high-energy electron. The lower energy photons, scattered by free electrons of much higher energy, gain energy in the interaction. The fractional energy transfer per scattering is

$$\frac{\Delta E}{E} = \frac{4kT}{mc^2},$$

where T is the electron temperature and m is the electron mass.

Synchrotron Emission

Synchrotron radiation is associated with the acceleration suffered by charged particles as they spiral around a magnetic field. Figure 1.3 illustrates the process. The rate of emission is inversely proportional to the product of the radius of curvature of the orbit and the fourth power of the mass of the particle. The force felt by a charged particle in a magnetic field is perpendicular to the direction of the field and to the direction of the particle's velocity. This causes the particle to spiral around the direction of the field, and since circular motion represents acceleration (i.e., a change in velocity), the electrons radiate photons of a characteristic energy corresponding to the radius of the circle.

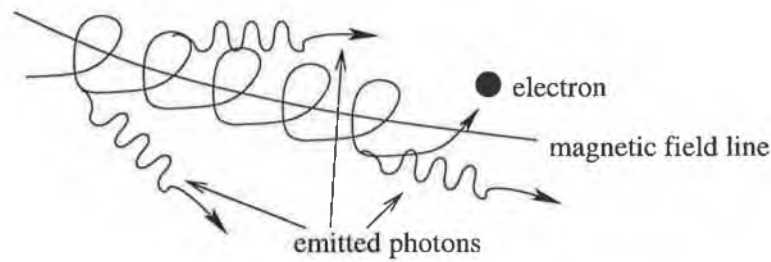


Figure 1.3: An illustration of synchrotron emission, where photons are emitted at tangents to the path of an electron spiralling around a magnetic field line.

Gamma Radiation Resulting from π^0 Decay

In addition to these electronic processes, gamma radiation can also occur as a result of proton interactions. For proton energies above 1.2GeV, interaction with nuclei produces unstable secondary particles, including π^0 mesons. The π^0 meson decays rapidly to a pair of gamma-ray photons, and the resulting gamma-ray spectrum has a characteristic maximum at around 70MeV, which corresponds to half the rest mass of the π^0 . For π^0 mesons travelling toward the observer at relativistic speeds, the corresponding photons are Doppler-boosted and their energies may reach the VHE range if the original photons are of sufficient energy.

All of the above processes which give rise to high-energy gamma radiation require the existence of extreme physical conditions, such as those expected to occur in the vicinity of exotic objects like supernovae, pulsars, black holes and active galactic nuclei (AGN).

1.3 Detection of Cosmic Gamma Radiation Using the Imaging Atmospheric Cherenkov Technique

For photon energies above a few MeV, the interaction length in matter is of the order of $30\text{g}\cdot\text{cm}^{-2}$. Since the Earth's atmosphere is about $1030\text{g}\cdot\text{cm}^{-2}$ thick, the only method of directly detecting high-energy cosmic gamma radiation is with space-borne instruments. Space-borne telescopes have the unavoidable problem of being constrained to small collection areas due to payload restrictions. The largest gamma-ray telescope flown to date was the very successful Energetic Gamma Ray Experiment Telescope (EGRET) on the Compton Gamma Ray Observatory (CGRO), where the effective collection area was only 0.15m^2 . All space-borne gamma-ray telescopes (SAS-II in 1973, COS-B in 1975 and EGRET in 1991) have a similar functional form and this trend is followed in the design of the Gamma-ray Large Area Space Telescope (GLAST), scheduled for launch in 2006. However, GLAST will use solid-state detectors (rather than the gas-filled detectors of previous missions), giving it a sensitivity two orders of magnitude higher than that of EGRET at energies above 1GeV.

Ground-Based Telescopes

High-energy gamma radiation is absorbed high in the Earth's atmosphere and cannot be detected directly at ground level. Ironically, however, the very atmosphere responsible for this can itself be used as a detection medium with high efficiency at very high energies. Air shower detection techniques give the possibility of detecting electromagnetic cascades with relatively simple detectors.

When a high-energy gamma-ray photon enters the upper atmosphere, it will penetrate only a short distance before undergoing pair production. In

this process, the photon materialises into an electron-positron pair:

$$h\nu \rightarrow e^+ + e^-.$$

The original photon no longer exists, its energy having gone to the two resulting particles. If the energy of the primary gamma-ray photon, and hence the electron-positron pair, is large enough, an electromagnetic cascade, known as an extensive air shower (EAS), will result, which will continue down through the atmosphere with secondary gamma-ray and electron production by bremsstrahlung and pair production as shown in Figure 1.4. The cascade

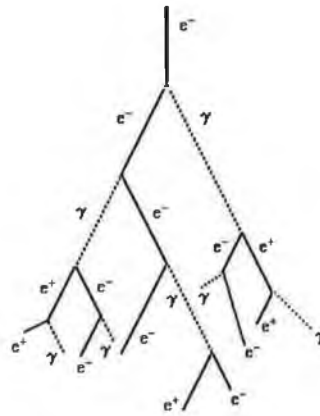


Figure 1.4: Part of an electromagnetic air shower, which produces a cascade of electrons, positrons, and further gamma rays.

will continue along the axis of the trajectory of the original gamma ray and the total energy of the secondary particles will be a good representation of its energy. The number of particles in the cascade increases geometrically until the mean electron energy falls below a critical energy ($\sim 85\text{MeV}$), at which energy loss by ionisation exceeds that of bremsstrahlung. At this point, the shower has reached its maximum development and, as it subsequently propagates lower in the atmosphere, the number of charged particles decreases exponentially (Ong 1998).

The particles created in this cascade are extremely energetic and, as such, they may travel at speeds exceeding the phase velocity of light in the medium

of the atmosphere. As a result, the medium in the immediate vicinity of the particle track is polarised and emits a faint bluish light known as “Cherenkov radiation”, named for the Russian scientist who studied the phenomenon (Cherenkov 1934).

The Cherenkov radiation is emitted at small angles to the particle direction in air. The Cherenkov opening angle, θ_{max} (the maximum angle of emission with respect to the direction of particle motion), is given by

$$\cos \theta_{max} = \frac{1}{\beta n}, \quad (1.4)$$

where $\beta = \frac{v}{c}$ (v is the particle velocity; c is the speed of light) and n is the refractive index of the medium.

This defines a minimum particle velocity, v , for which Cherenkov emission can occur in any given medium:

$$\beta n \geq 1 \implies v \geq \frac{c}{n}. \quad (1.5)$$

For air with refractive index 1.000283 (Allen 1979), the velocity must therefore exceed $0.9997c$. For electrons, the corresponding energy is 22MeV.

Figure 1.5 illustrates the emission of Cherenkov radiation from an air shower. Each particle that causes Cherenkov radiation emits light along a small cone. Superposition of all the radiation from all the particles in the shower gives rise to a thin flat light pool propagating in the direction of the shower axis. The Cherenkov production spectrum varies as λ^{-2} , where λ is the photon wavelength. Since the atmosphere is largely transparent to light between 300nm and 600nm, most of the produced Cherenkov radiation reaches the ground under good atmospheric conditions. For example, a 1TeV gamma-ray shower results in an average of about 3×10^6 Cherenkov photons at ground level. The Cherenkov photons are strongly beamed in the forward direction and they preserve the directional information contained in the shower particles. Most of the radiation is produced from particles near the shower maximum. The lateral distribution of Cherenkov light is therefore determined largely by the altitude of the shower maximum and

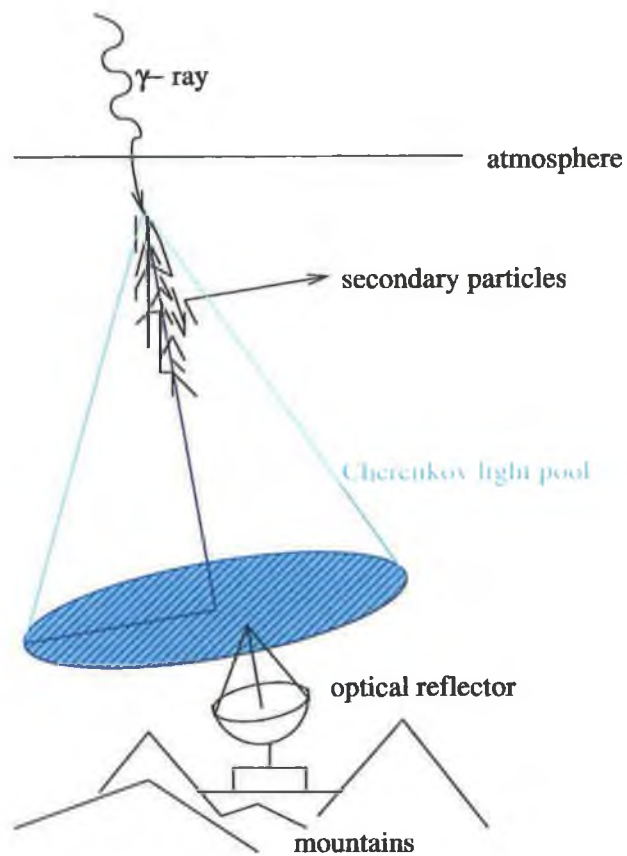


Figure 1.5: A gamma-ray induced electromagnetic air shower producing Cherenkov radiation, detected by an atmospheric Cherenkov radiation detector.

the Cherenkov opening angle. For vertically incident gamma rays of energy 1TeV, shower maximum occurs at an average altitude of 8km (Ong 1998). At this altitude, the Cherenkov angle is approximately 1.2° so that, for an observatory at an altitude of 2km, the light pool on the ground extends relatively uniformly over a radius of about 125m. This corresponds to an area of approximately $5 \times 10^4 \text{m}^2$ and a Cherenkov detector within this pool has an effective collection area of this scale. Using the atmosphere as a detector therefore dramatically increases collection area in relation to satellite-borne detectors (compare 0.15m^2 for EGRET).

Imaging Detectors

The detection of gamma rays using the atmospheric Cherenkov technique requires discrimination between actual gamma-ray induced air showers and the much more numerous air showers generated by incident charged cosmic-ray particles (primarily protons). A generic atmospheric Cherenkov telescope uses a mirror to concentrate Cherenkov light from an air shower on to a single photomultiplier (PMT) tube or on to a camera consisting of an array of PMTs. An array of tubes essentially allows an image of the shower to be taken using the Cherenkov light produced by the shower. A list of the major imaging atmospheric Cherenkov telescopes currently in operation and their main characteristics is shown in Table 1.3. The Whipple Observatory system is described in more detail in Section 1.4.

1.4 The Whipple Observatory Gamma-Ray Telescope

The Whipple collaboration operates a ten meter light collector on Mount Hopkins, Arizona, 2320m above sea level. The reflector was originally constructed in 1968 (Weekes 1972) and numerous modifications have been made since then to improve the sensitivity and performance of the system (Fe-

Group	Location	Aperture	Camera Pixels	Threshold	Epoch
				TeV	Beginning
Whipple	Arizona, USA	10m	490	0.25	1984
GT-48	Crimea, Ukraine	6 × 2.4m	6 × 37	1	1985
SHALON	Tien-Shan, Russia	4m	244	1.0	1994
CANGAROO	Woomera, Australia	3.8m	256	0.5	1994
HEGRA	La Palma, Spain	5 × 3m	5 × 271	0.5	1994
CAT	Themis, France	3m	600	0.25	1996
TACTIC	Mount Abu, India	10m	349	0.3	1997

Table 1.3: Imaging atmospheric Cherenkov telescopes currently in operation.

gan et al. 1983; Cawley et al. 1990). The reflector's current configuration, shown in Figure 1.6, is based on a Davies-Cotton design (Davies & Cotton 1957) and uses 248 tessellated, front-aluminised mirrors, which produce high-quality images over a wide field of view.



Figure 1.6: The current Whipple ten metre telescope in its stowed position.

During the summer and autumn of 1999, a 490-pixel high-resolution camera was installed in the focal plane of the reflector. A full description is given by Finley (2001). The camera (shown in Figure 1.7) consists of an inner

camera populated by 379 13mm PMTs, surrounded by 111 28mm PMTs. The field of view (FOV) of the inner camera is 2.6° in diameter, while the overall FOV has diameter 4.0° .

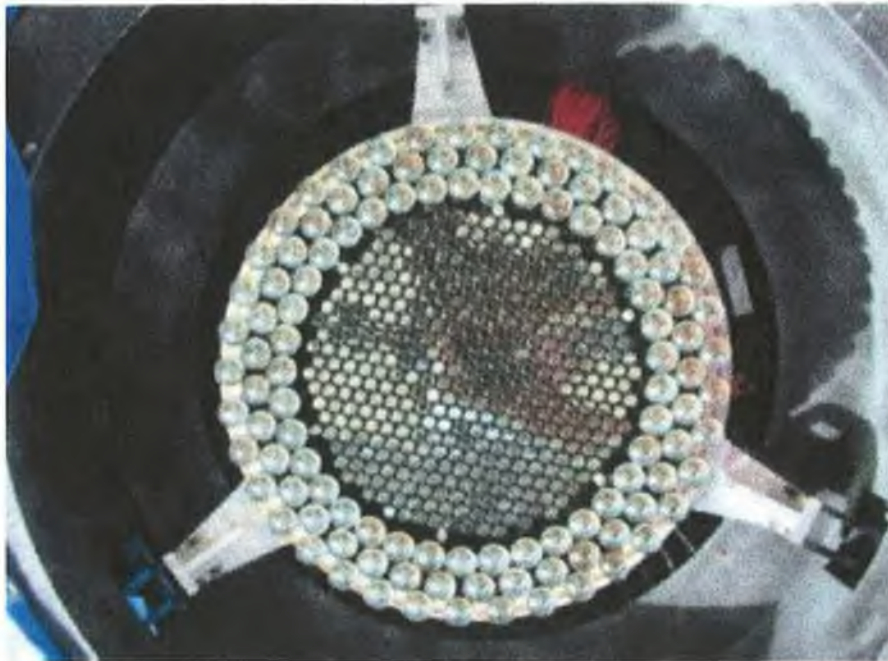


Figure 1.7: The Whipple ten metre telescope GRANITE III, 490-pixel camera. Note the inner camera, comprising 379 13mm PMTs, and the three outer rings of 28mm PMTs.

The Whipple Collaboration has been instrumental in establishing the existence of four TeV gamma-ray sources (the Crab Nebula, Markarian 421, Markarian 501 and 1ES1959+650) at significance levels in excess of 10σ . The analysis techniques used by the Whipple Collaboration to establish these sources is discussed in Chapter 4, and the most recently confirmed of the sources, the AGN 1ES1959+650, is discussed in detail in Chapter 5. The EGRET experiment, operating with an upper energy limit of 30GeV, detected 129 gamma-ray sources (Thompson et al. 1995). Bridging the large energy gap between the EGRET upper energy bound and the current lower energy bound of 300GeV for atmospheric Cherenkov detectors is a major

objective for the next-generation of ground-based systems. The lower energy threshold offered by next generation telescopes will allow the study of possible spectral breaks in emission from AGN, the search for pulsed gamma-ray emission from pulsars and the detection of more distant and weaker sources. One such next generation detector is the Very Energetic Radiation Imaging Telescope Array System (VERITAS).

1.5 The VERITAS Project

The atmospheric Cherenkov technique can be significantly improved by the use of multiple telescopes with separations of the same order as the lateral spread of light from the shower. This technique has been effectively demonstrated using pairs of telescopes (Krennrich et al. 1998) and arrays (Konopelko 1999). The reduction in energy threshold is less than that achieved by combining all the mirror area into one telescope, but the distribution of mirror area into multiple telescopes gives many images of the same shower, which offers other advantages. These include improved hadron discrimination from multiple image characterisation, elimination of local muon background, improved energy resolution from multiple measurements, shower axis location, determination of shower maximum and improved angular resolution (Weekes et al. 2002).

VERITAS is a proposed array of seven large imaging telescopes, which are improved versions of the existing Whipple ten metre imaging telescope (Weekes et al. 2002). The seven identical telescopes will be arranged in a hexagonal layout with one telescope at the centre as shown in Figure 1.8. The telescopes will each have a camera consisting of 499 PMTs and a FOV 3.5° in diameter. The FOV is chosen as the minimum required for individual telescopes to reconstruct images from point sources. The focal length chosen is 12m, corresponding to $f/1.2$ for an aperture of 10m. This represents an increase in focal length compared with the Whipple 10m telescope's $f/0.7$, thereby improving optical quality by reducing the effect of off-axis aberra-

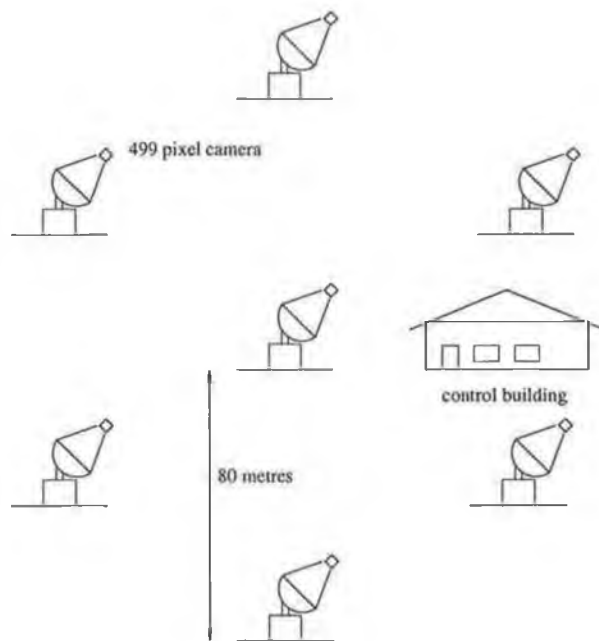


Figure 1.8: The proposed layout of the seven VERITAS telescopes.

tions. An engineering sketch of a VERITAS telescope is shown in Figure 1.9.

The parameters of the array are chosen to give optimal flux sensitivity in the 100GeV–10TeV range which has proved to be rich in scientific returns, but also with significant sensitivity in the ranges 50–100GeV and 10–50TeV. The predicted flux sensitivity is a factor of ten better than any other detector in this range. Figure 1.10 shows a plot of flux sensitivity, $F(E > E_t)$, versus threshold energy, E_t , for a range of gamma-ray detectors including Whipple and VERITAS. $F(E > E_t)$ represents the number of photons per cm^2 per second with energy, E , above the threshold, E_t .

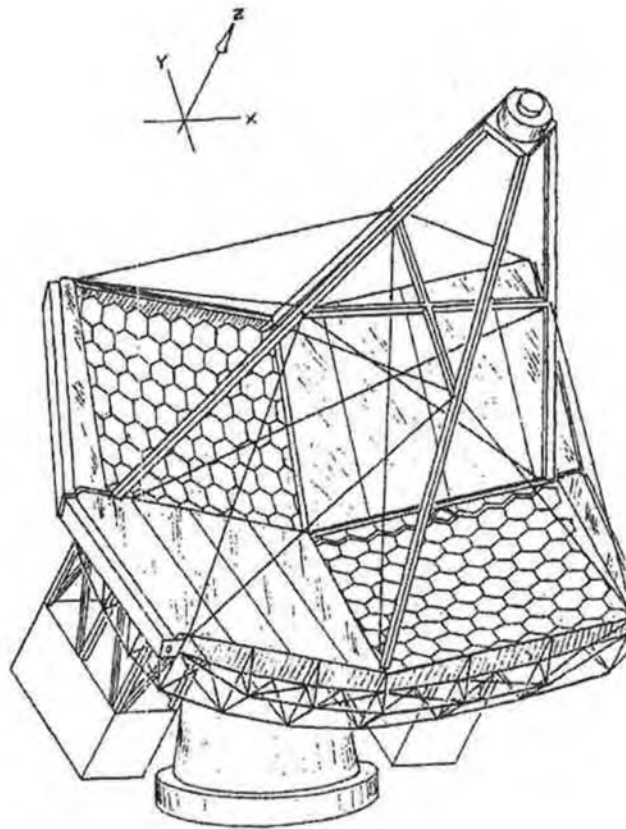


Figure 1.9: An engineering sketch of a VERITAS telescope.

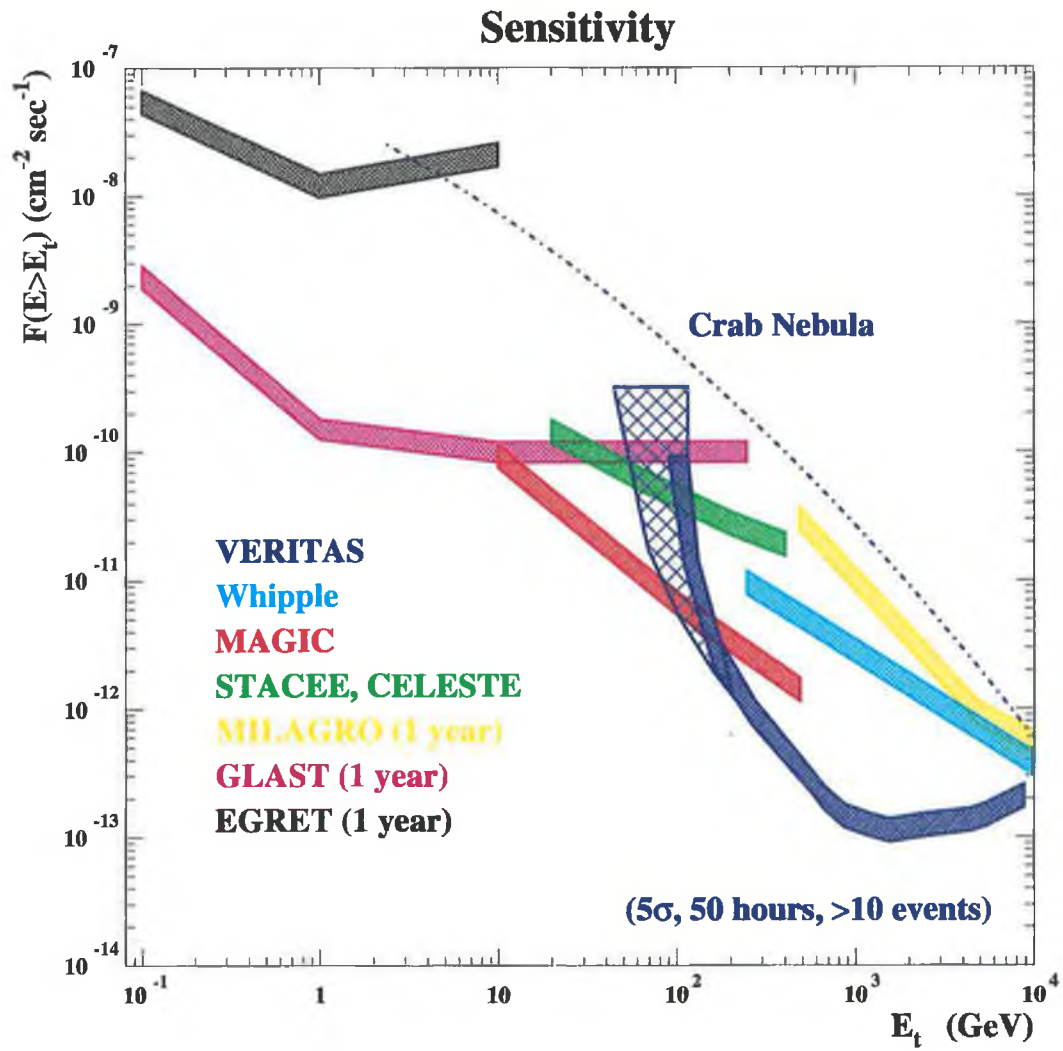


Figure 1.10: The flux sensitivities of various gamma-ray detectors.

1.6 Sky Monitoring Instrumentation for VERITAS

The VERITAS telescopes will detect the Cherenkov radiation emitted from air showers occurring at altitudes of the order of 8km. Transmission of the Cherenkov light through the atmosphere is strongly influenced by the optical clarity of the atmosphere and the prevailing weather conditions. The performance of the telescopes is therefore dependent on atmospheric effects. In order to quantify such effects, the VERITAS proposal envisages sky monitoring instrumentation, comprising a CCD camera and a far infrared (FIR) pyrometer, mounted on each telescope. A prototype sky monitoring system, developed for this purpose at GMIT and Cork Institute of Technology, was successfully installed and tested on the existing Whipple 10m telescope during the period April–June 2002. Chapter 2 describes in detail the hardware associated with this system, and the software developed to operate it is described in Chapter 3.

Chapter 2

Prototype Instrumentation for the VERITAS Project

2.1 Introduction

Observations of atmospheric Cherenkov radiation are optimally made in dark, cloudless and moonless skies. A long-standing problem in measuring this radiation has been the need to monitor the clarity of the atmosphere through which the observations are made - the radiating medium of the Cherenkov light. There have been a number of different approaches to the problem of monitoring the transparency of the night sky. These include laser probing the atmosphere and measuring the scattered light (Abu-Zayyad et al. 1997), and monitoring the complete hemisphere using a matrix of mid-infrared radiometers (Bird 1997). Any reduction in atmospheric transparency reduces the proportion of Cherenkov light which reaches a ground-based detector from an extensive air shower, and consequently the number of events which trigger the detecting system is reduced. The detection rate for cosmic ray background events is therefore correlated with atmospheric conditions.

The following two chapters of this thesis present the hardware and software involved in implementing two different methods of quantifying the prevailing weather conditions in the field of view of the Cherenkov telescope.

One method is based on using a far infrared (FIR) pyrometer to monitor the temperature of the night sky in the direction of observations, while the other uses a CCD camera to monitor the brightness of stars in the field of view of the Cherenkov telescope.

For evaluation purposes, a Santa Barbara Instrument Group (SBIG) ST-237 CCD camera and a Heitronics KT-15.82D FIR pyrometer were purchased, and the prototype systems were installed and commissioned on the existing Whipple ten metre atmospheric Cherenkov telescope as a testbed for the VERITAS project.

2.2 The CCD Camera

A CCD (charge-coupled device) is a solid-state imaging detector arranged in a rectangular array of imaging elements (pixels). Such detectors are commonly used in video cameras and have been used for astronomical imaging for over twenty years. CCDs are particularly useful for astronomical imaging because they can image small faint objects, which would otherwise require long film exposures. They have several advantages over photographic film, including short exposure times, quantitative accuracy (arising from linear integration of intensity) and the availability of direct computer interfaces. The last feature means that digitised images can be downloaded and stored for subsequent manipulation and enhancement as required.

2.2.1 Principle of Operation of the CCD

The basic function of a CCD detector is to convert incoming photons of light to electrons, which are stored in a detector array, with the accumulated charge read out after a suitable exposure time. A CCD must perform four tasks in generating an image:

- **Charge Generation:** Quanta of light incident on the array of metal oxide semiconductor (MOS) capacitors that make up the CCD chip generate

electron-hole pairs. The number of pairs generated is proportional to the number of incident quanta.

- **Charge Collection:** The photoelectrons are collected in the nearest discrete collecting sites or pixels. The collection sites are defined by an array of electrodes, called gates, formed on the CCD, so that during an exposure to light, a “charge packet” accumulates at each electrode.
- **Charge Transfer:** This is accomplished by manipulating the voltage on the gates in a systematic way so the charge packets move down the vertical registers from one pixel to the next. At the end of each column is a horizontal register of pixels, the readout register. This register collects the charge packets from one line at a time and transports the packets from this line in a serial manner to an on-chip charge amplifier as shown in Figure 2.1.
- **Charge Detection:** The charge amplifier converts each individual charge packet to output voltage levels representing the light intensity at the corresponding pixel position. The voltage for each pixel is further amplified off-chip and digitally encoded using an analogue-to-digital converter (ADC). The digitised values can then be stored in computer memory for subsequent reconstruction and display on a computer monitor screen.

Dark noise or dark current is the result of thermally generated electrons building up in the CCD pixels during an exposure. The number of electrons due to dark noise is related to the integration time for the exposure and the temperature of the CCD. The longer the exposure time and the higher the temperature of the CCD, the greater the resulting amount of noise. Two precautions are taken to minimise the effects of dark noise in the image. One is simply to cool the camera and the other is to subtract the noise by using a “dark frame”.

The CCD itself generates thermal noise caused by the operation of the electronics on the chip. The goal in cooling the CCD is to minimise unwanted

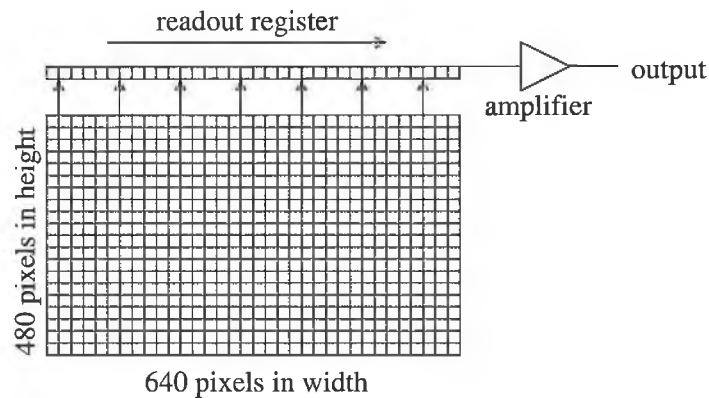


Figure 2.1: A CCD chip reading out an image from its array of electrodes. The values are transferred vertically one line at a time and then transported serially via the readout register to the on-chip amplifier.

sources of electron production in the chip and thus make the detector more sensitive to the electrons produced by the incoming photons. For every 8°C reduction in temperature, the dark current in the CCD is reduced by half, so that cooling from ambient temperature to below 0°C can reduce the dark current by an order of magnitude. A thermoelectric (TE) cooler (a Peltier cell) mounted on the back of the CCD chip is used to perform the task of cooling the CCD. This acts as a heat pump; when electric current is passed through it, heat is pumped via the TE cooler out of the CCD. A fan can then be used to move the resulting hot air out of the CCD unit.

To reduce further the effect of this significant source of noise in the images, a dark frame is used. A dark frame is usually taken using the same integration time and at the same temperature as the image for which it is to be used. It is taken under conditions as close as possible to complete darkness, usually achieved by closing the shutter wheel on the camera. The dark frame can then be subtracted from the normal exposure, or light frame, to minimise any dark noise inherent in the image.

2.3 Installation of the SBIG ST-237 CCD Camera

The ST-237 CCD camera uses a Texas Instruments TC237 CCD chip with 640×480 pixels, each measuring $7.4\mu\text{m} \times 7.4\mu\text{m}$. The chip has an overall active area of $4.7\text{mm} \times 3.6\text{mm}$ and uses double-correlated sampling with a 12-bit ADC for the readout. It requires a 12V DC power supply capable of delivering a current of 1.2A. The large current is required to drive the Peltier cooler used for temperature reduction.

The CCD camera (and the FIR pyrometer) are encased in a durable metal housing, designed and constructed at the National University of Ireland, Maynooth (courtesy of Dr. Michael Cawley). Suitable clamps were included in its design to allow it to be attached to one of the arms which support the focus box of the Whipple ten metre telescope (see Figure 2.5) and provision was made for the housing to be rotated in the horizontal plane for directional adjustments. The camera can also swivel on a ball joint on its mount inside the housing to allow for small vertical and horizontal adjustments. A transparent glass window in the housing in front of the camera, protects it from dust and moisture, without obstructing its field of view (FOV). Figure 2.2 shows two views of the housing with the top cover removed. The picture on the left shows a plan view, with the FIR pyrometer to the left and the CCD camera to the right. The picture on the right is a side view, with the FIR pyrometer in the foreground and the CCD camera behind it.

The CCD camera's FOV is considerably larger than that of the telescope, so the CCD is aligned to point in the direction of the telescope's optic axis. Figure 2.3 shows a diagram of the fields of view for the CCD and for one of the VERITAS telescopes. It is not essential that the centre of the FOV of the CCD coincide precisely with the optic axis of the telescope as long as the offset is known. Alignment was achieved by pointing the telescope at a known star (e.g., Polaris) then, using a cross-hair at the centre of the CCD image, an estimation was made as to how far off-centre the star was.



Figure 2.2: Two views of the CCD camera and FIR pyrometer in their protective housing (with the top cover removed for purpose of photograph).

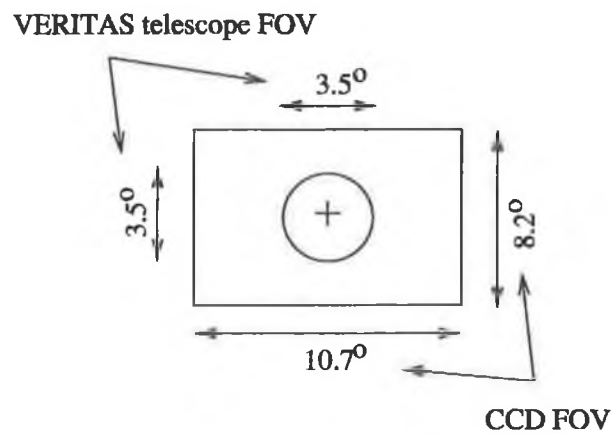


Figure 2.3: The CCD camera FOV (represented by the rectangle) and a VERITAS telescope FOV (represented by the circle).

The telescope was then returned to its rest position and the CCD camera's pointing direction was adjusted appropriately. This process was repeated until the star image was sufficiently close to the centre of the image.

Precise alignment is difficult, as the vertical and horizontal adjustments of the camera are uncalibrated. Initial alignment was intended only to establish pointing to within $\sim 1^\circ$. Flexure of the telescope is highly correlated with the elevation of observations, so the pointing accuracy of the CCD varies as the telescope moves. For CCD images taken when the ten metre telescope was pointed in the direction of the Crab Nebula, the position of the Nebula was found to be within 0.5° of the centre of the CCD FOV. An offset of this magnitude is quite acceptable for this application.

During monsoon season (July–September) at Mount Hopkins there is a considerable risk of lightning storms. The telescope electronics are therefore at risk of being damaged during this period. To safeguard against this, a tall lightning conductor is erected beside the telescope (see Figure 2.4 to right of the telescope), but this not a 100% guarantee of protection. The CCD camera housing contains expensive hardware and the best way to protect this from lightning damage is to remove all electrical connections when lightning is imminent/expected. This requirement influences the choice of position for the housing. It was originally positioned on the right side arm of the telescope (see Figure 2.4); this required the use of a ladder for access, making it potentially unsafe in the event of lightning. It was therefore moved to the more easily accessible bottom arm of the telescope such that in the event of lightning, observers can simply walk to the back of the housing and disconnect all of the cables (see Figure 2.5).

The CCD camera is controlled and powered via a parallel cable from a central processing unit (CPU). This CPU requires a 12V DC power supply rated at 1.2A and is encased in a box with two parallel cable connectors available at the side. One of these is connected to the host computer and the other to the camera itself. This is illustrated in Figure 2.6. Previous CCD monitoring systems installed at the ten metre telescope have been connected

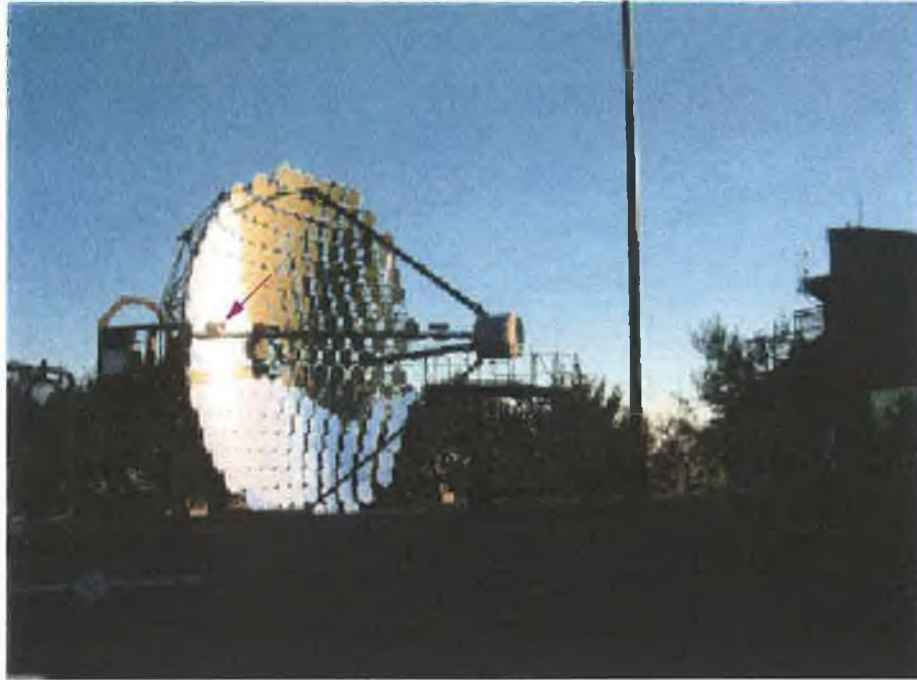


Figure 2.4: The CCD camera/FIR pyrometer housing in its original position (arrowed) on the side arm of the Whipple ten metre telescope.



Figure 2.5: The CCD camera/FIR pyrometer housing box mounted on the bottom arm of the Whipple ten metre telescope (left view and front view; arrowed).

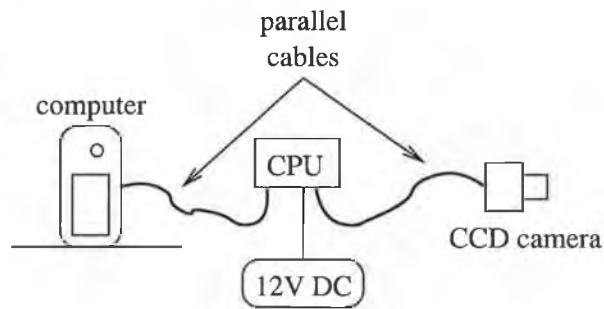


Figure 2.6: A diagram of the CCD camera connected to its CPU, which in turn is connected to a computer.

directly to a computer inside the observing building. In the design described here, the CCD connects to a computer inside the telescope mount and XML communication is used to transmit the information via Ethernet from that computer to a computer in the observer building. This reduces the need for excessively long cables. However, in the original design of the housing, provision was made to allow the CCD CPU to be positioned in a section underneath the camera. The parallel cable would even then have to run over a distance greater than that recommended for parallel communications in order to connect from the CPU in the housing to the computer inside the telescope mount. To overcome this problem, additional driver circuits were incorporated so as to permit communication over longer distances. When the system is installed for the VERITAS project, this may prove necessary, but for prototyping purposes, the cables are sufficiently long to allow the camera to be connected to the computer in two stages as illustrated in Figure 2.7. The CCD CPU is now positioned on a platform at the centre of the telescope's optical support structure (OSS). Cables run from there, down through the centre of the telescope's mount to the computer which controls the camera and acts as a server from which the CCD data can be read. This is described in more detail in Chapter 3.

A Fujinon model CF25L lens was chosen for the CCD camera. This lens has an adjustable f -number, from $f/0.85$ to $f/11$, and for the CCD it is set to the lowest f -number, $f/0.85$, such that bright images can be obtained over a

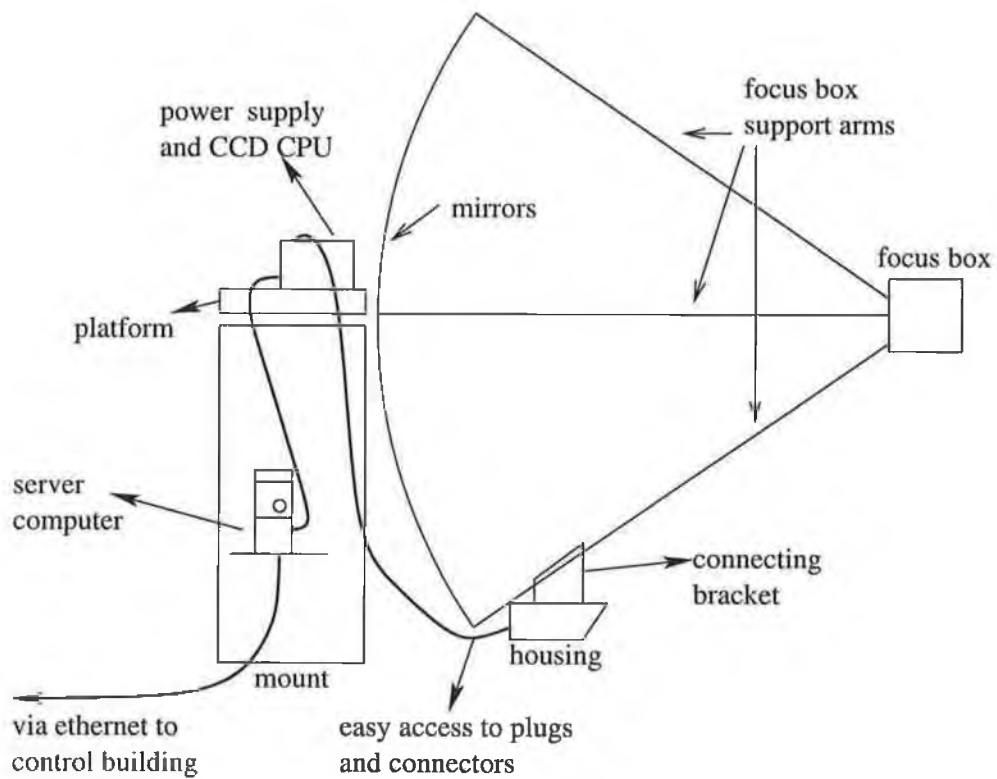


Figure 2.7: A diagram of the CCD camera in its housing, connected to the mount computer in two stages.

wide field of view. A wide field of view is desirable so a larger area of sky than that imaged by the VERITAS telescopes is monitored. To accommodate this special lens, the inner aperture in the front plate of the camera was enlarged to 24.2mm in diameter and the built-in shutter wheel had to be removed as it prevented the lens from focusing for large object distances. This had the effect of moving the lens closer to the CCD chip, so that the nominal focus distance (as indicated on the lens barrel) does not correspond to the actual object distance which is in focus. Focusing on stars in the night sky (infinity) was therefore achieved by using successive approximations. An image of the night sky was taken and checked for focus; if the image was not sharply in focus the lens's focus was adjusted and another image was taken. This process was repeated until the star images were adequately focused, which was found to correspond to a nominal setting of approximately 2.5m on the lens focus ring. Figure 2.8 shows a picture of the CCD camera with the $f/0.85$ lens in its housing mounted on the side arm of the Whipple ten metre telescope.

2.4 CCD Camera Results

For the CCD with an active area of $4.7\text{mm} \times 3.6\text{mm}$ and the lens with a focal length of 25mm, the FOV can be calculated from $2 \tan^{-1} \left(\frac{4.7/2}{25} \right) \times 2 \tan^{-1} \left(\frac{3.6/2}{25} \right)$, which means the FOV is approximately $10.7^\circ \times 8.2^\circ$ (see Figure 2.9). The CCD has 640×480 pixels, which means the angle per pixel is very close to $1'$ in the horizontal and vertical making angular measurements in the images very convenient.

Figure 2.10 shows the result of a ten second exposure using the CCD camera of the star field in the direction of the active galaxy 1ES1959+650. This image was compared to precision star charts such as can be generated with software package like *Cartes Du Ciel* (Chevalley 2001), *Xephem* (Downey 2002) or *KStars* (Harris et al. 2001). For example, Figure 2.11 shows a chart generated using *KStars* for the star field in the same direction and at the



Figure 2.8: The focused CCD camera mounted in its housing on one of the side arms of the Whipple ten metre telescope. The housing cover was removed for the purpose of illustration.

4.7mm x 3.6mm CCD chip

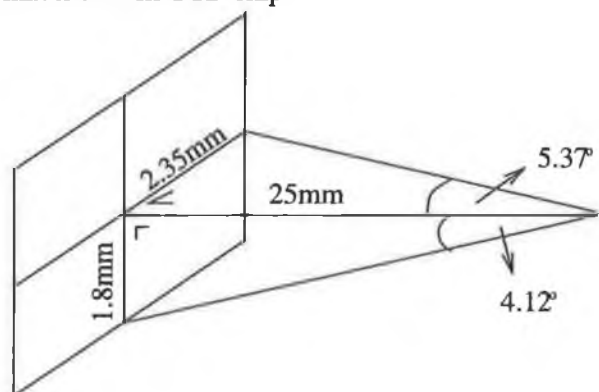


Figure 2.9: Calculation of the CCD's field of view.

same time as that in Figure 2.10. Comparing these images confirmed that the CCD has a field of view of approximately 10.7° horizontally by 8° vertically. Careful examination of the CCD image shows that, for exposures of this duration (i.e., ten seconds), stars down to 9th magnitude or fainter can be identified.



Figure 2.10: A ten second CCD exposure using an $f/0.85$ lens on the star field in the direction of 1ES1959+650 (RA = 19h 59m, Dec. = $65^\circ 00'$).

Figure 2.12 and Figure 2.13, respectively, show a CCD image and a star-chart image (generated using *KStars*) of the star field in the direction of the Crab Nebula. The Crab Nebula with a diffuse magnitude of 8.4 is at (or near) the centre of both images. It is marked in the star-chart image, but is only visible with image enhancement in the CCD image. Some of the stars in the images are labelled with their names and magnitudes, and the planet Saturn, with magnitude -0.25 , appears in both images but is at the extreme edge of the CCD FOV. The star ζ Tauri, with a magnitude of 3.0 is the bright star near the centre of the image and some of the other stars in the constellation of Taurus are labelled, most notably 119 Tau and 114 Tau with magnitudes 4.38 and 4.88, respectively. Clearly, the CCD camera is performing as expected in providing excellent images of the star field. A more

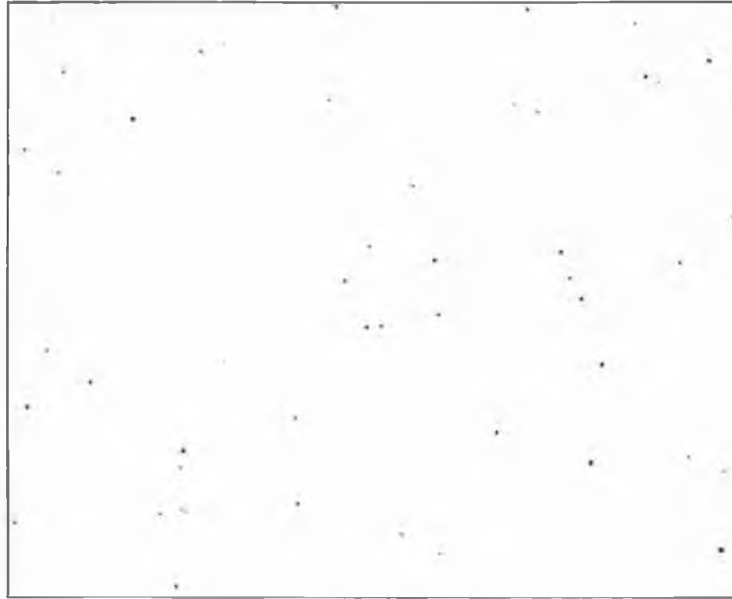


Figure 2.11: A star chart generated using *KStars* software for the star field in the direction of 1ES1959+650 (RA = 19h 59m, Dec. = 65°00').

detailed discussion of the CCD star images in relation to the magnitudes of the imaged stars is given in Section 3.4.1.

2.5 The FIR Pyrometer

Thermal radiation is emitted by all materials at temperatures above the absolute zero point (i.e., zero Kelvin). The relationship between temperature and peak emission wavelength is discussed in Section 1.2. From Equation 1.1, it can be seen that at 5700K, the surface temperature of the Sun, the peak wavelength emitted is in the blue/green part of the visible spectrum at 508nm. For lower temperatures, peak emission shifts into the infrared region of the spectrum: at 100°C the spectrum peaks at 8 μ m, while at -50°C the peak occurs at 13 μ m. Instruments that measure this radiation and provide an output signal calibrated in temperature units are called radiation thermometers or radiation pyrometers and the determination of temperatures by non-contact measurement of thermal radiation is called radiation pyrometry.

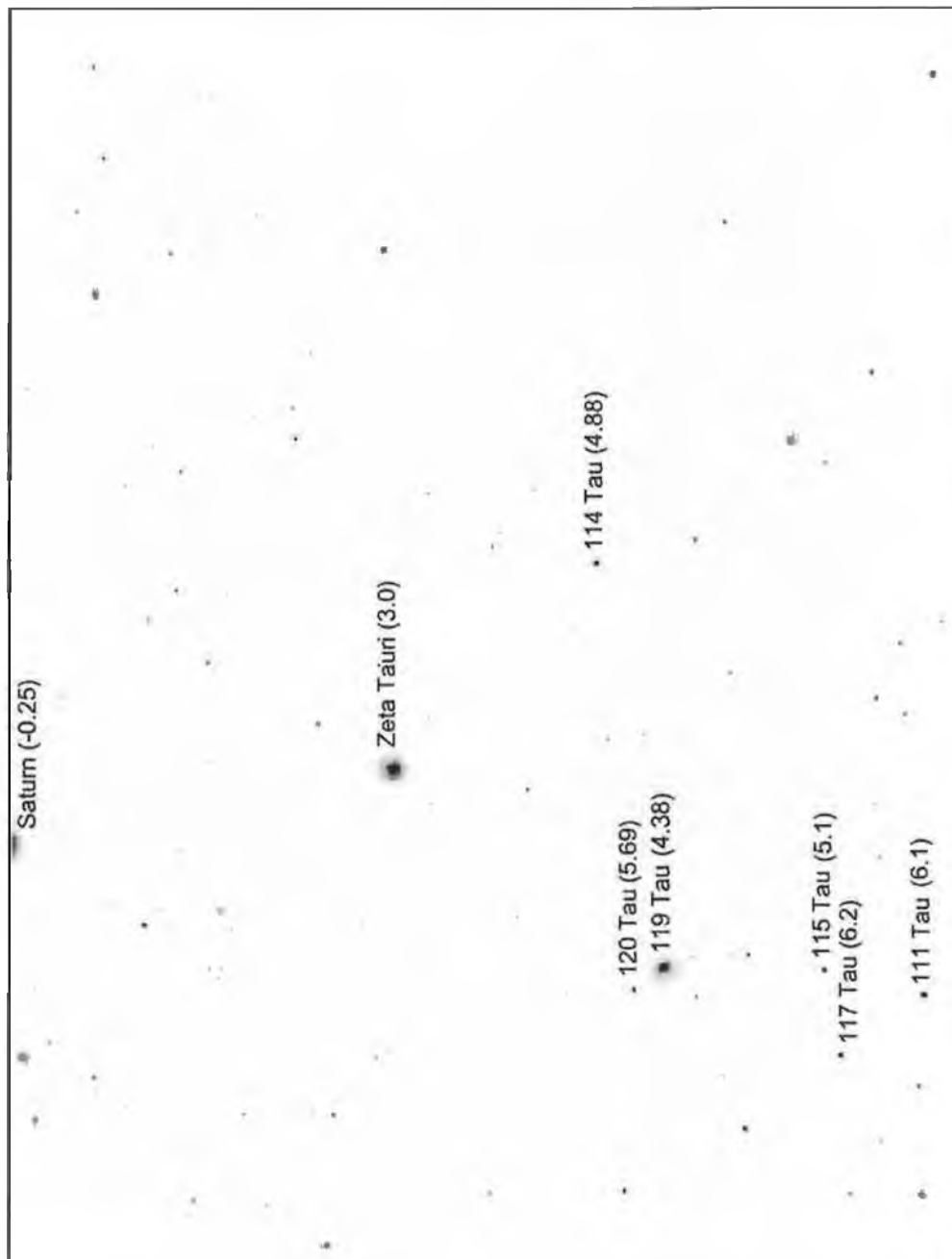


Figure 2.12: A ten second CCD exposure using an $f/0.85$ lens on the star field in the direction of the Crab Nebula (RA = 5h 31m 34.4s, Dec. = 21°58'40.2"). The numbers in brackets are the stellar magnitudes. A star chart for the same field is shown in Figure 2.13.

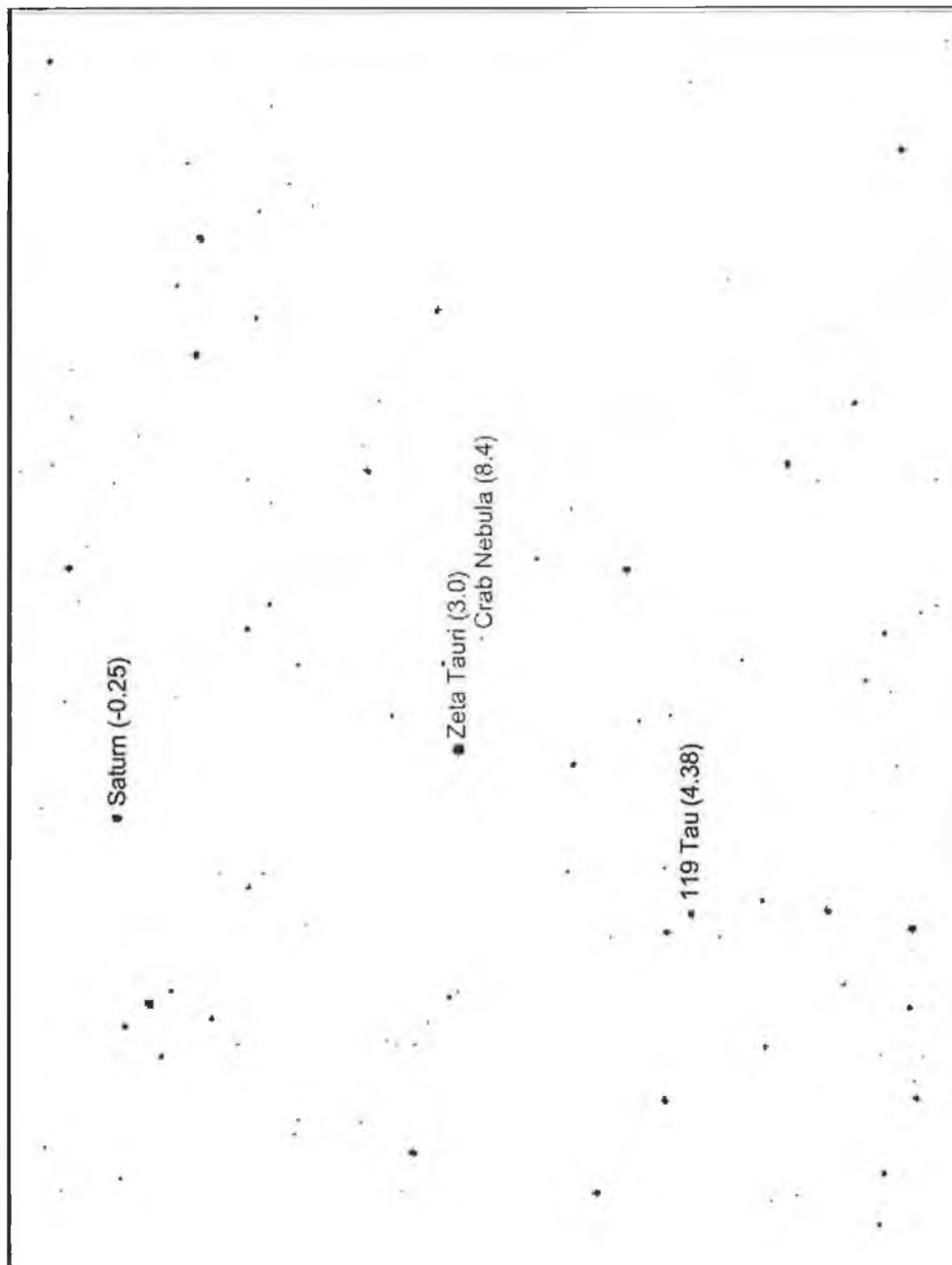


Figure 2.13: A star chart generated using *KStars* software for the star field in the direction of the Crab Nebula (RA = 5h 31m 34.4s, Dec. = 21°58'40.2"). The numbers in brackets are stellar magnitudes. The field shown is approximately the same as that in Figure 2.12. The solid line which runs across the field is the ecliptic.

2.5.1 Infrared Pyrometry

It is a well-known experience that thermal radiation emitted by objects can be felt by the thermal sensors in our skin. Radiation pyrometers quantify this effect by using a measuring transducer that receives radiation emitted by the object or objects in its field of view and transforms it into a standardised output signal. If the emissivity (see Section 2.5.2) of the object in question is known, the temperature of the object can be determined. A radiation pyrometer essentially provides a measurement of the equivalent blackbody brightness temperature of the scene in its field of view. It is not an imaging device: the output from the pyrometer represents an *average* temperature for all surfaces within its FOV. The non-contact character of the measurement makes the pyrometer an ideal instrument for many applications. These include glass forming, thin-film plastic manufacturing, LCD display fabrication, and (for the VERITAS weather monitoring system) cloud detection.

Clouds offer a hindrance to the propagation of Cherenkov radiation in the atmosphere and as such it is important when measuring this radiation to be aware of their presence. Cloud temperatures are in general higher than the temperature of a clear night sky, so when a cloud enters the field of view of a radiation pyrometer, an increase in the reported temperature should be observed. How much the temperature increases depends on the height and thickness of the cloud and on the amount of water vapour in the atmosphere between the instrument and the cloud. Low heavy clouds generally produce the largest increase in temperature, especially in winter when the clear sky temperature is very low; high thin clouds produce a lesser increase. When there is no cloud within the field of view of the instrument, the clear sky temperature depends almost entirely on the amount of water vapour in the atmosphere above the instrument.

2.5.2 Emissivity

The radiant emittance from a blackbody, R_B , is proportional to the fourth power of the temperature, T (Stefan-Boltzmann law).

$$R_B = \sigma T^4, \quad (2.1)$$

where $\sigma = 5.67 \times 10^{-8} \text{Wm}^{-2}\text{K}^{-4}$ is the Stefan-Boltzmann constant. R_B represents the theoretical maximum radiant emittance from a surface at any given temperature, but real surfaces in general fall short of this. The emissivity, ε , of a surface is defined as the ratio of the radiant emittance of the surface to that of a blackbody at the same temperature. For a real surface, therefore, the radiant emittance is given by

$$R_B = \varepsilon \sigma T^4, \quad (2.2)$$

The value of ε ranges between 0 and 1, where $\varepsilon = 1$ corresponds to a blackbody and $\varepsilon = 0$ defines a perfect "thermal mirror". Factors which affect the value of the emissivity include the geometrical shape of the surface and the uniformity of the temperature. The emissivity is also in general temperature-dependent.

2.5.3 The Heitronics KT15D Series Pyrometers

The versatile KT15D series infrared pyrometer was chosen as a suitable model for the purpose of measuring the temperature of the night sky. A photograph of this model is shown in Figure 2.14 and a summary of its main specifications and settings is given in Table 2.1.

The unit offers a choice of 12 different lenses for near and far focusing. The model for the VERITAS prototype uses the K6 germanium lens (see Table 2.1), which is transparent to far infrared radiation. This lens provides a field of view of $\sim 2.8^\circ$, which is similar to the fields of view of the current Whipple ten metre telescope and the proposed VERITAS telescopes. The instrument's FOV was deliberately kept smaller than those of the telescopes because of its non-imaging characteristics, which average over the

Specification	Value
Power Requirements	22–30V DC or 24V AC $\pm 10\%$, 48–400Hz
Spectral Response	8–14 μm
Communications	RS232
Weight	0.55kg
Lens/FOV	germanium/ $\sim 2.8^\circ$
User Definable Setting	Range
Emissivity	0.1–1.0
Ambient Temperature	-50°C to $+100^\circ\text{C}$
Temperature Units	$^\circ\text{C}$, $^\circ\text{F}$, K
Response Time	50ms–10s
Transfer Rate	1200–19200bps

Table 2.1: Summary of the main specifications for the KT15D FIR pyrometer.

entire FOV. The lens itself is fragile, so to shield it from unnecessary exposure to the elements, the housing (Section 2.3) incorporates a protective shutter which is retracted by means of a solenoid when power is supplied to the unit. A glass window cannot be used to protect the pyrometer as this would cause the unit to measure the temperature of the glass in front of it and not that of the night sky. The spectral response range of 8 μm –14 μm for the KT15.82D provides for temperature measurement from -60°C to $+110^\circ\text{C}$, with highest reliability between -50°C and $+100^\circ\text{C}$.

The KT15D pyrometer’s choice of emissivity settings allows the use of the unit for temperature measurement of surfaces whose thermal emissions deviate from that of a perfect blackbody (Table 2.1; Figure 2.17). For the clear night sky, ϵ is expected to be very close to 1. The KT15D also allows account to be taken of the ambient temperature as a governing factor for its sky temperature reading (see Figure 2.17). The user can allow the pyrometer itself to read the ambient temperature using an in-built thermometer; alter-



Figure 2.14: The Heitronics model KT15D infrared pyrometer.

natively the user can specify the ambient temperature setting, which allows for setting between -50°C and $+100^{\circ}\text{C}$. The response time of the unit can be set between 50ms and 10s. This value affects the total integration time used to judge the temperature of objects in the FOV and how quickly information is updated for the user. Shorter integration times allow the detection of highly variable weather conditions over short time scales, whereas longer integration times allow for a more accurate average temperature reading.

A KT15.82D FIR pyrometer was installed at the Whipple ten metre telescope. Figure 2.2 shows a picture of the pyrometer in its protective housing with the CCD camera. The pyrometer is controlled via a standard 9-pin RS232 interface (Figure 2.15). The signals transmitted or received via the

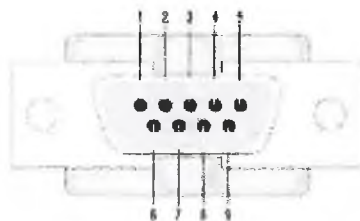


Figure 2.15: The RS232 standard interface pin out.

pins labelled in Figure 2.15 are described in Table 2.2.

An RS232 cable running from the CCD/FIR housing, up the back of the

Pin #	Signal
1	Data Carrier Detect
2	Received Data
3	Transmitted Data
4	Data Terminal Ready
5	Signal Ground
6	Data Set Ready
7	Request to Send
8	Clear to Send
9	Ring Indicator

Table 2.2: Pin-outs for RS232 communications.

telescope and down through the telescope mount, to the computer inside the mount, connects the pyrometer to the server computer (the cable was subsequently replaced by a fibre optic connection, which performs the same task, but offers extra lightning protection for the FIR pyrometer). This is the same server computer to which the CCD camera is connected. A schematic of the pins used to connect the RS232 interface of the server computer to that of the FIR pyrometer is shown in Figure 2.16.

2.5.4 FIR Pyrometer Results

As suggested by Buckley et al. (1999), a major factor governing the measurement of sky temperature is the temperature of the air at observation level. To investigate this dependence and the effect of varying the emissivity setting used, the pyrometer was set up to point at one of the walls of the control building. The ambient temperature setting for the pyrometer was manually set to fixed values and the values of emissivity used were varied. Figure 2.17 shows a plot of the results. These results do not represent measurements where the actual ambient temperature or emissivity of the object were changing, rather they represent the effects of changing the pyrometer settings. It is clear that increasing the ambient temperature setting causes

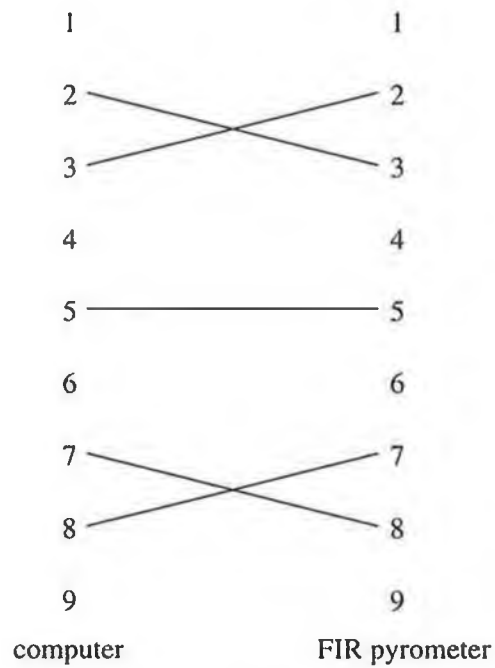


Figure 2.16: The pins used in the RS232 interface to control to FIR pyrometer.

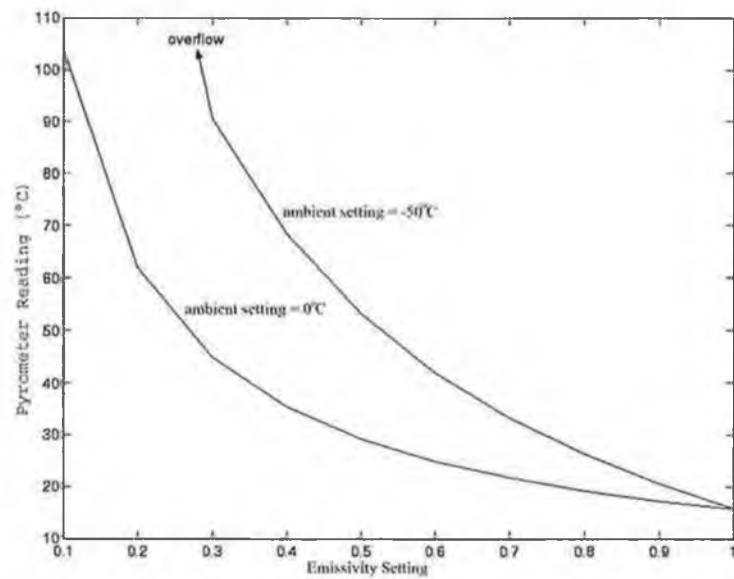


Figure 2.17: Graph of temperature read from FIR pyrometer versus emissivity setting for varying ambient temperature settings.

the temperature reading to decrease and increasing the emissivity setting also causes it to decrease. For an emissivity setting of 1.0, the ambient temperature setting has no effect on the temperature read out by the pyrometer. For the present application, where the primary concern is determination of the clear sky temperature, the emissivity was set to 1.0. With an emissivity setting of 1.0, accurate cloud temperatures cannot be expected to be measured, but their presence are still detected.

Figure 2.18 shows how effective the pyrometer is at detecting cloud in its FOV. The data was taken on the morning of September 12th, 2002 whilst pointing at the zenith. A clear spike in the data is visible when a cloud drifted in and caused the temperature reading to rise sharply. When the cloud moved on, the temperature dropped as sharply again, back to the its value before the cloud entered the FOV. For these data, the temperature was recorded every 30 seconds and the integration time was 3 seconds.

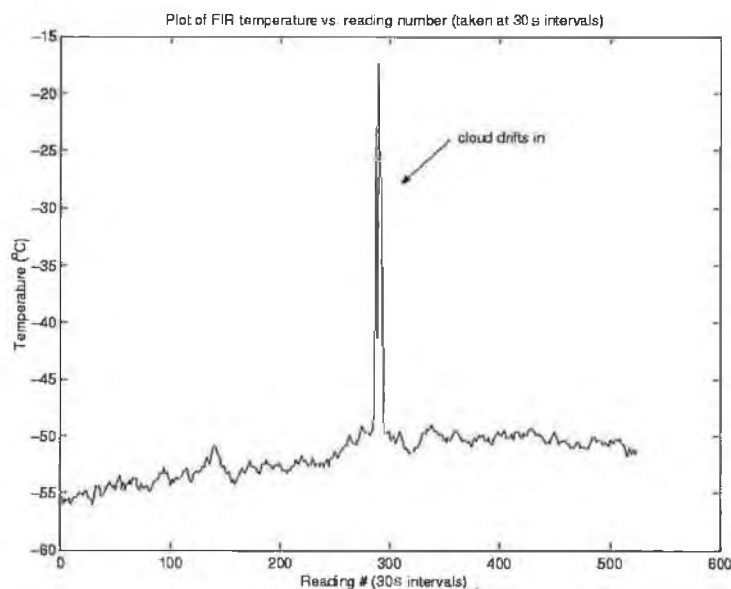


Figure 2.18: Plot of FIR pyrometer temperature readings while pointing to zenith at the ten metre telescope on the morning of September 12th, 2002.

As mentioned in Section 2.5.1, the raw rate of the data coming from the telescope (which essentially represents the detection rate for cosmic-ray in-

duced showers) is dependent on the prevailing weather conditions in the field of view of the telescope. To investigate the correlation between the temperature reading from the FIR pyrometer and this cosmic-ray rate a number of contemporaneous data sets were taken. Figure 2.19 and Figure 2.20 show the cosmic-ray rate and the FIR pyrometer readings respectively, for data taken in the direction of a potential gamma-ray source, the galaxy NGC 4736, on the evening of June 12th, 2002. The x-axis shows the elapsed time in seconds for both runs; the y-axis in Figure 2.19 shows the raw cosmic-ray data rate and the y-axis in Figure 2.20 shows the FIR pyrometer temperature readings. It can be seen that a dip in the raw rate approximately 400

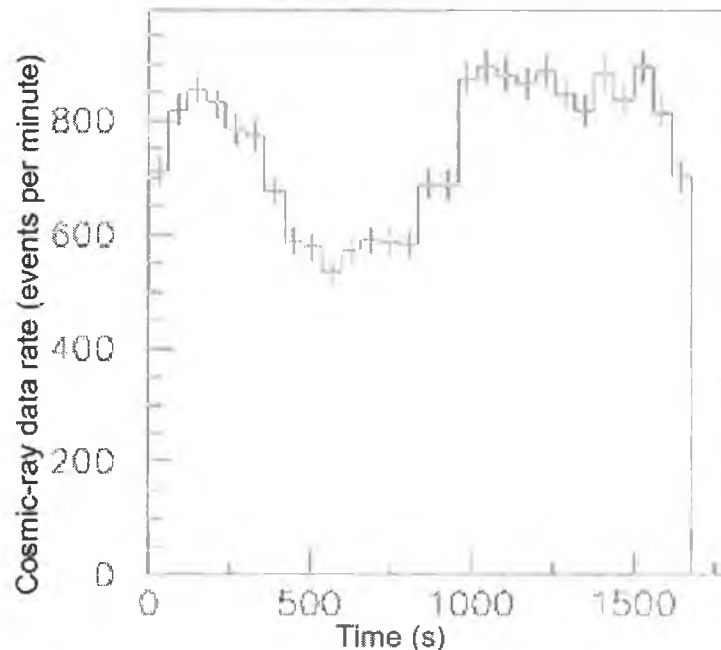


Figure 2.19: Raw cosmic-ray data rate recorded with the Whipple ten metre telescope while pointing at NGC4736 from UT 05:11 to 05:41 on June 12th, 2002.

seconds into the run correlates well with a rise in the measured sky temperature at the same time. When the weather improves again at around 900 seconds, the FIR pyrometer reading falls and the cosmic-ray rate rises. This indicates that the pyrometer is effective in performing the task of weather

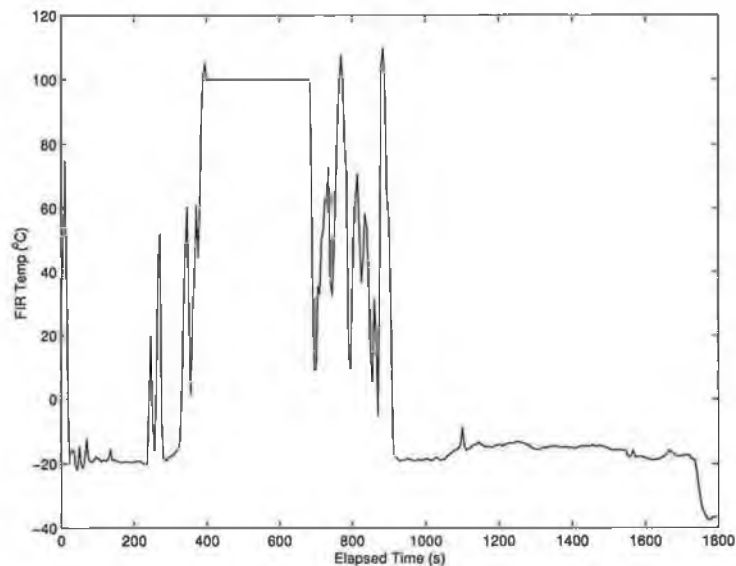


Figure 2.20: FIR pyrometer temperature readings while pointing at NGC4736 from UT 05:11 to 05:41 on June 12th, 2002. The time interval for these data is the same as for data in Figure 2.19.

monitor. Figure 2.21 and Figure 2.22 show data taken in the direction of the TeV gamma-ray source 1ES1959+650 on June 7th. These show a cosmic-ray data rate from the telescope of approximately 700 events per minute, rising slightly as the run progresses, and the corresponding FIR pyrometer readings dropping from -33°C to -38°C , over the same time interval. Both plots are consistent with a slight but gradual improvement in weather conditions over the duration of the run. To illustrate the overall consistency of the FIR pyrometer's measurements, Figure 2.23 shows a plot of FIR pyrometer readings for two separate 30 minute runs on different nights, where the raw cosmic-ray event rates were similar at $\sim 850\text{--}900$ events per minute. The two FIR pyrometer data plots show similar behaviour, indicating that the readings are consistent from night to night.

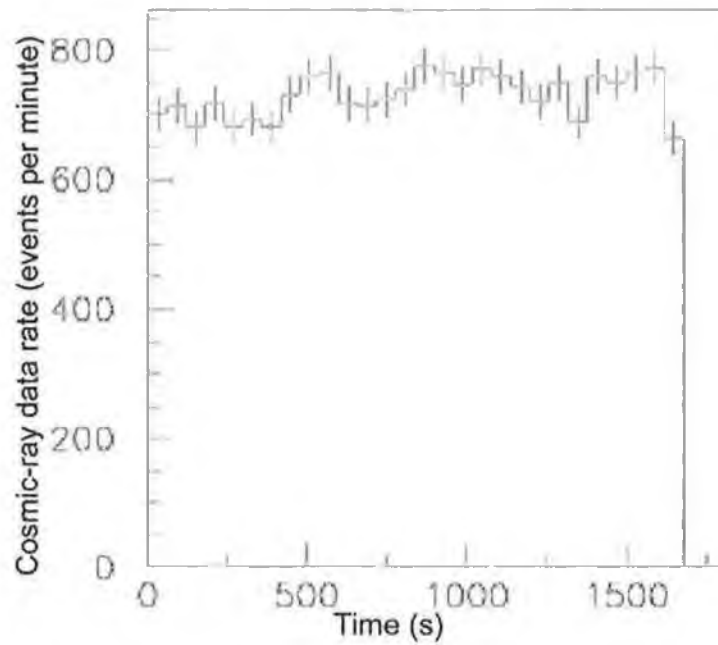


Figure 2.21: Raw cosmic-ray data rate from the Whipple ten metre telescope while pointing at 1ES1959+650 from UT 07:43 to 08:11, June 7th, 2002.

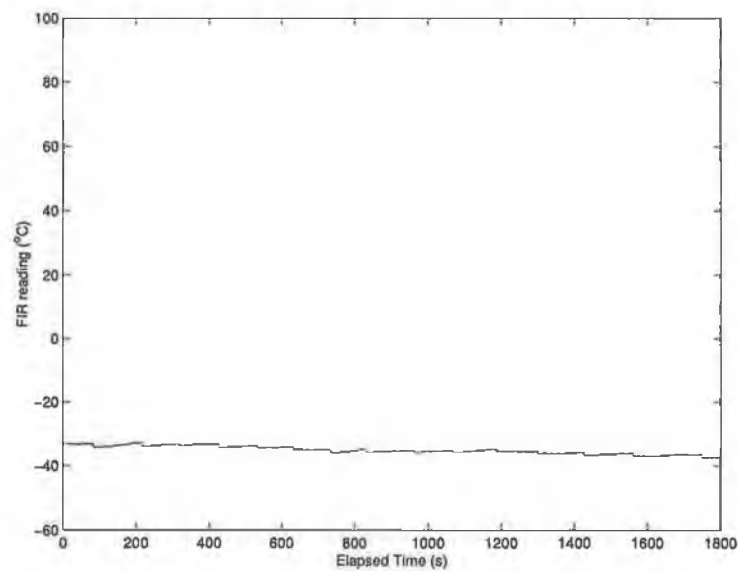


Figure 2.22: FIR pyrometer temperature readings while pointing at 1ES1959+650 from UT 07:43 to 08:11 on June 7th, 2002. The time interval for these data is the same as for data in Figure 2.21

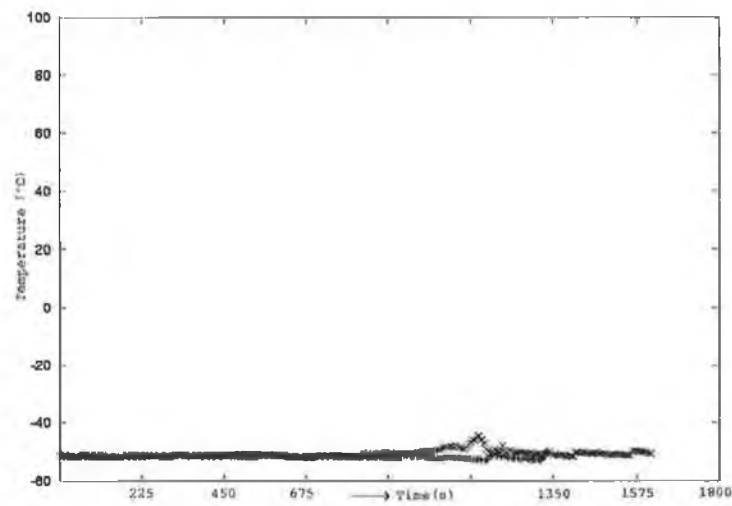


Figure 2.23: Comparison of FIR pyrometer temperature for two separate runs with similar raw cosmic-ray data rates (~ 900 events per minute).

Chapter 3

Prototype Software for the VERITAS Project

3.1 Introduction

VERITAS is a large project, consisting of members from institutions in Ireland, England and the USA. Hardware and software development is divided among these different institutions and, as such, it is necessary to define specific standards to which these tasks must comply. Redhat LINUX was chosen as the standard operating system on which all software developed must run and C++ was chosen as the standard programming language, using the Qt graphical user interface (GUI) toolkit for all GUI-related features. Qt, distributed by Trolltech™ (<http://www.trolltech.com>), is a multi-platform C++ GUI application framework. It provides application developers with all the functionality needed to build applications with state-of-the-art graphical user interfaces. Qt is fully object-oriented, easily extensible, and allows true component programming.

Many software tasks in the project require computers on a network to communicate with one another, therefore requiring a standard communications package. All communications software written for this thesis uses XML (eXtensible Markup Language) messages, sent over the network using Trans-

mission Control Protocol/Internet Protocol (TCP/IP).

3.2 XML Over TCP/IP

The approach of using XML messages sent via TCP/IP was originally chosen to perform the task of inter-machine communication in the VERITAS project. An alternative to this approach is to use CORBA (Common Object Request Broker Architecture) from the Object Management Group (OMG® <http://www.omg.org>) to manage communications. Both of these approaches use a client/server architecture to send and receive data¹.

3.2.1 Client/Server Communications

Clients and servers are essentially computers that listen on designated ports for connections from other computers. Ports are used in computers for communications and are numbered from zero upward, depending on the computer's architecture. Some of these ports are reserved for processes such as Hyper-Text Transfer Protocol (HTTP) and electronic mail (e-mail), so for an application like the one considered here, unused ports are chosen for the client and server and information is transferred between these ports. The server computer is connected to the device from which the data comes (e.g., the CCD camera) and the client computer is connected to a computer monitor, which displays the information in the form of a GUI, although a GUI is not always necessary. This layout is illustrated in Figure 3.1.

Like HTML (Hyper-Text Markup Language), XML is a subset of SGML (Standard Generalised Markup Language). XML data consists of character data and markup text. Markup text is enclosed in angle brackets (< and >) and character data is the text between a start tag and an end tag. For example, in the following XML message, <markup> is the start tag, </markup> is the end tag and the text "This is character data" is the character data.

¹Note added in proof: A collective decision was subsequently made to use CORBA as the VERITAS communications standard.

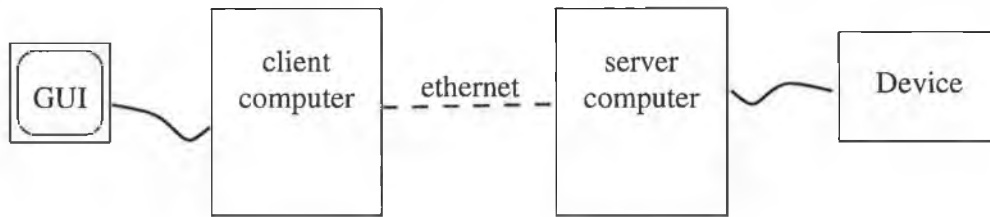


Figure 3.1: A client computer and display, communicating with a server computer, which is connected to a device that reads out data.

<markup>This is character data</markup>

Figure 3.2 shows the various stages of communication in the client and server software. On the client side is a generic XML client, which is the same for all devices using the software. This receives data from, and passes data to, an XML message handler, which is custom written for each device so that it knows what data to expect. The device display is the GUI that displays the relevant information for the particular device. The handler can receive data from the device display (in the form of a request for data) or from the XML client (in the form of the data returned from a request). Having decided from the XML tags what data it has received, the handler calls the relevant function in the client (in the case where a request is to be made) or the GUI (in the case where received data is to be displayed). On the server side, a generic XML server performs a similar task to the client, but requests for data are passed from the handler to the device API (application programming interface), which returns the requested information.

The software for the XML clients and servers uses *Simple API for XML* (SAX) to access XML documents' contents. SAX-based parsers invoke responses ("methods") when markup text is encountered (e.g., start tags or end tags). These parsers are available for a variety of programming languages including Java. Trolltech™ have adapted the parser for Java to comply with Qt naming conventions and since Qt was used for all the VERITAS GUI software, it naturally followed to use the XML module provided in the Qt package. Using the C++ feature of inheritance, custom responses can be pro-

it undesirable to use (<http://doc.trolltech.com/3.1/signalsandslots.html>). In the signal/slot method for communication between objects, a “signal” is “emitted” whenever a particular event occurs. In the pushbutton example above, a signal containing information that the button was pushed is emitted. This signal is connected to a “slot”, which is a function called in response to the signal. Hence, in the code, each of the desired signals is connected to a specific slot which performs a predetermined task. Below is an excerpt from the code controlling the CCD camera. When the user clicks on the pushbutton `fQuitPB` in the GUI display window, a `clicked()` signal is emitted and this is connected to the object `qApp`, which contains the predefined slot `closeAllWindows()`. The overall effect is that clicking on the `fQuitPB` pushbutton results in all windows in the display being closed down.

```
connect( fQuitPB, SIGNAL(clicked()), qApp, SLOT(closeAllWindows()) );
```

Using the C++ feature of inheritance, complicated GUIs can be built up from the predefined widgets included in the Qt package. To use a general example, if a programmer wanted to define objects which describe a set of cars of various makes and models that can be used in a computer game, he/she might first define an object which has the attributes of a general car such as a steering wheel, four wheels, brakes, etc. Sub-classes, which inherit these features may then be defined, such as Ford and Subaru, and these could again be sub-classed to make the Fiesta and the Impreza class, respectively. The Fiesta class would then have all the attributes of a Ford and all the attributes of a car as well as some of its own specific attributes. Similarly in Qt, the features of a `QWidget` are inherited by a `QPushButton`, the features of a `QPushButton` are inherited by a `QPushButton`, and a `QPushButton` included in a GUI can be customised to look and act as desired (constrained by the features available to a `QPushButton`, which includes the features available to a `QPushButton` and a `QWidget`; see Figure 3.3).

Figure 3.4 an example of the code to create a basic widget with only one pushbutton using Qt; Figure 3.5 shows a screen-shot of the widget that this produces. For any GUI application that uses Qt, there is precisely one

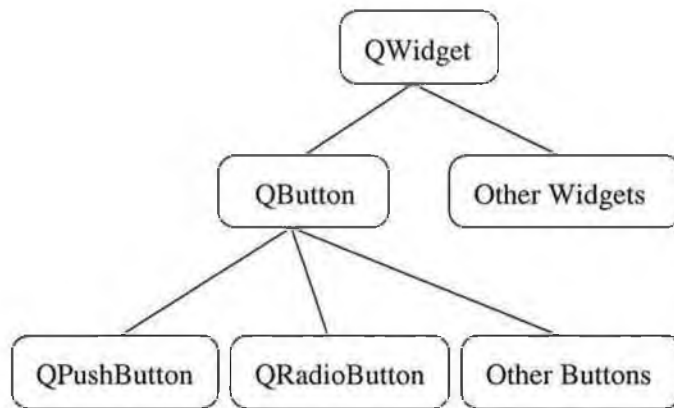


Figure 3.3: An illustration of how inheritance is used in Qt widgets.

```

#include <qapplication.h>
#include <qpushbutton.h>

int main( int argc, char **argv )
{
    QApplication a( argc, argv );
    QPushButton hello( "Hello world!", 0 );
    hello.resize( 100, 30 );
    hello.setCaption("QPushButton Example");
    a.setMainWidget( &hello );
    hello.show();
    return a.exec();
}

```

Figure 3.4: Example of the code used to create a basic widget using Qt.



Figure 3.5: A screen-shot of a basic Qt widget with only one pushbutton, entitled “Hello world!”.

`QApplication` object. This contains the main event loop, where all events from the window system and other sources are processed and dispatched. It also handles the application initialisation and finalisation, and provides session management. In Figure 3.4, a `QApplication` object named `a` is created on line 1 of `main`. On line 2, a pushbutton called “hello” is created, with arguments to specify the legend to appear on it in the GUI (“Hello World!”) and its parent widget, which in this case is “0” (i.e., it has no parent, so it is a top-level widget). Various options are then set (`hello.resize(100, 30)` and `hello.setCaption("QPushButton Example")`), and the pushbutton `hello` is set to be the main widget. Finally, `a.exec()` is executed; this enters the main event loop and waits until `exit()` is called, whereupon it returns to `main` the value to which it was set (0, if it was called via `quit()`). The program then exits.

Figure 3.6 shows an excerpt from the header file for the code which defines the appearance of the CCD control panel developed for the CCD GUI in this project. Two pushbuttons, `fContinuousPB` and `fSinglePB`, are defined as private members of the class `CCDControls`, and two signals, `signalContinuous()` and `signalSingle()`, are defined as signals belonging to the class. The button `fContinuous` is intended to begin a process which continuously takes CCD images, and `fSinglePB` is intended to take just one CCD image. When the pushbuttons are created later on in the code, the `clicked()` signal from `fContinuousPB` is connected to `signalContinuous()` and the `clicked()` signal for `fSinglePB` is connected to `signalSingle()`.

```

#ifndef CONTROLS_H
#define CONTROLS_H

#include <qvgroupbox.h>
class QPushButton;

class CCDControls : public QVGroupBox{
    Q_OBJECT
public:
    CCDControls( const QString & title, QWidget * parent=0 );
    ~CCDControls();

signals:
    void signalContinuous();
    void signalSingle()

private:
    QPushButton *fContinuousPB, *fSinglePB;
};

#endif

```

Figure 3.6: An excerpt from the header file which defines the appearance of the CCD control panel developed for the CCD GUI used in this project.

This creates a new custom widget, which contains two pushbuttons and emits two different signals depending on the button pressed. Many more buttons or objects of any type can be created and added in to this custom widget, but in this example only two buttons are used. Figure 3.7 shows a screenshot of the custom widget used in the CCD camera control software. This

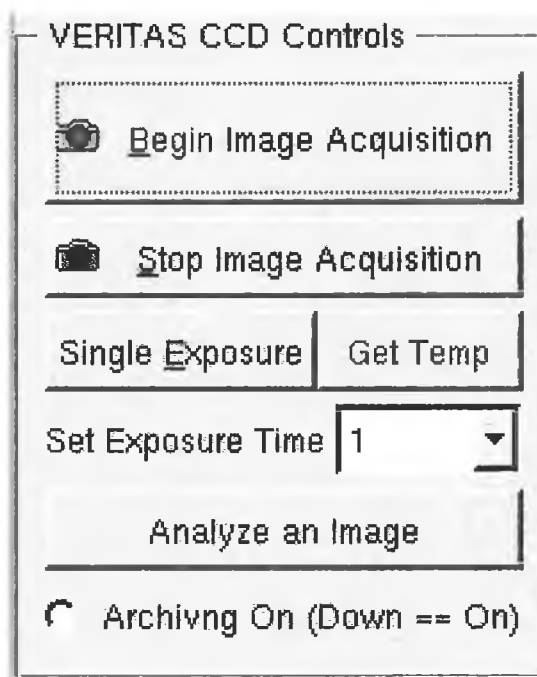


Figure 3.7: A screen-shot of the custom widget, which is used in the CCD client GUI (Figure 3.12).

widget contains 5 `QPushButton`s, a `QRadioButton` (beside `Archiving On`), 2 `QLabels` (`Set Exposure Time` and `Archiving On (Down == On)`), and a `QComboBox` (with the number 1 displayed), all of which have one or more of their pre-defined signals (defined in the Qt package) connected to a custom signal belonging to the class. The class `CCDControls` publicly inherits `QVGroupBox`, which essentially allows the individual widgets to be easily arranged vertically within the custom widget. This class can then be included in a larger widget and have its signals (e.g., `signalContinuous`) connected to different signals or slots as necessary.

As part of the weather monitoring project, code was also developed to control a weather station located on the roof of the observing building ². A screen-shot of the widget used to display its data is shown in Figure 3.8. This

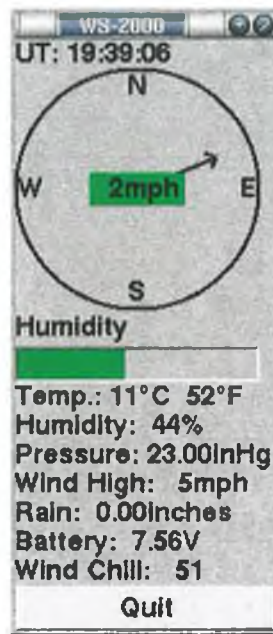


Figure 3.8: A screen-shot of the custom widget, which is used in the weather station client GUI.

widget is made up of several custom and Qt pre-defined widgets, including the custom-designed compass at the top. Data are read from the weather station using an RS232 interface. The data are in the form of a string which contains each data element (temperature, humidity, etc.), and this string is parsed to extract the individual values. One of these values is the wind direction and this is passed to the compass widget along with the wind speed. The compass widget then handles the display of the wind data by passing the direction data to a `QPainter`, which draws an arrow pointing in the appropriate direction,

²Primary responsibility for the installation and maintenance of the weather station devolves on University College Dublin. However, the development of the GUI is included in the present work because it forms a natural part of the overall communication and display software.

and the speed data to a `QLabel`, which updates the speed display. Figure 3.9 shows the layout of the classes used to define the GUI. This is an example

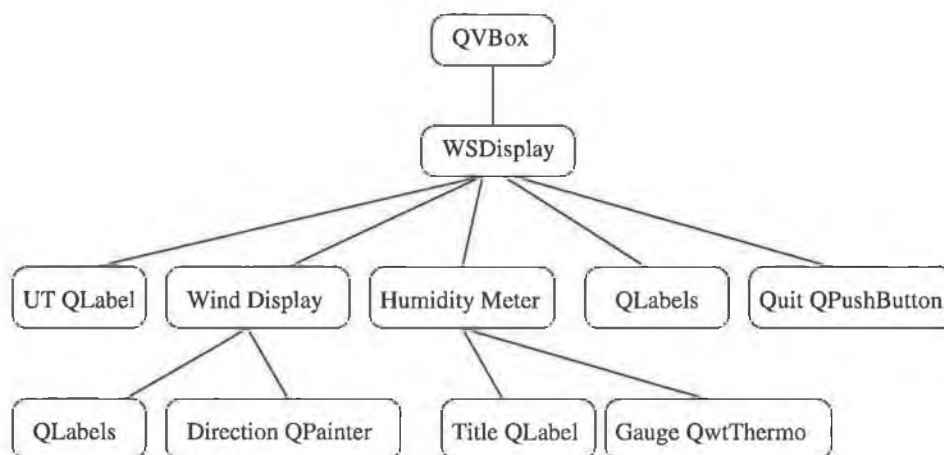


Figure 3.9: Illustration of the hierarchy for the weather station GUI class.

of object-oriented programming, which is an extremely powerful feature of C++. It has allowed the design of this project to be split into smaller, more manageable ones, which are subsequently combined and add up to make the finished product.

3.4 The CCD Camera Software

The SBIG ST-237 CCD camera is operated as part of the prototype sky monitoring system for VERITAS as described in Chapter 2. A proprietary LINUX driver distributed by the manufacturer (SBIG) controls the camera. This driver code was written in C, so a C++ wrapper was written such that it could be accessed using the C++ standard. Accessor functions like `connectToCamera()` and `exposeCamera()` are defined and interface with the original driver, making the control of the camera in software very user-friendly.

The CCD camera is connected to a computer in the telescope mount and is controlled remotely by a computer inside the observer building using the

XML communications package described in Section 3.2. Within an XML message, only character data may be used - integer values such as those representing pixel brightness in the CCD images are not allowed. The CCD images from the camera consist of a 640×480 array of 12-bit pixel values, so some means of converting this into character data is necessary.

Base-64 Image Encoding

To include the CCD images in the XML messages they are first encoded as base-64 text. The base-64 alphabet, which consists of the characters A-Z, a-z, 0-9, + and /, is widely used to convert integer data into ASCII characters. Each 12-bit pixel value is taken and split into two 6-bit values. Each 6-bit value is then expressed as a character from a member of the base-64 alphabet ($2^6 = 64$) as illustrated in Figure 3.10, where the value 101100001010 is converted into rJ, r being character 44 in the base-64 alphabet and J being character 10. In this process, each 12-bit pixel value in the image is converted into two ASCII characters (8 bits each). The encoded image is then inserted in the character data section of the XML message and sent to the client, where it is decoded using the same base-64 alphabet.

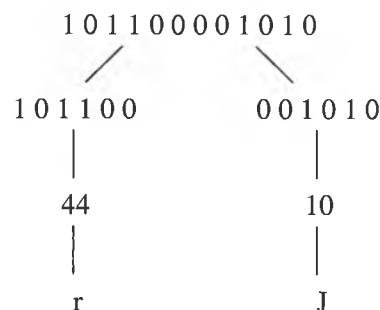


Figure 3.10: An example of the base-64 encoding process

The images are then displayed in the image window of the GUI on the client computer. They are also archived (if the archiving option in the GUI is turned on) using a custom image file format, which consists of a small header followed by the individual pixel values for the image, as shown in Figure 3.11.

Each 12-bit pixel value is stored as two bytes (16 bits) making each archived image 614442 bytes ($\sim 600\text{kB}$) in size. The filenames are generated from the UT date and time at the time of writing. A file stored on June 13th at 08:53:52 for example, would be named `d06_13_08_53_52.ccd`.

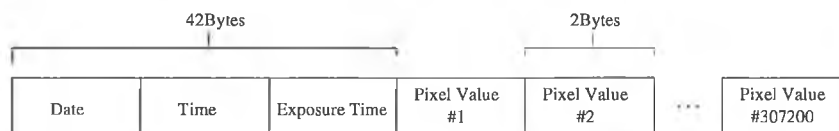


Figure 3.11: Format of an archived image file.

The CCD GUI was developed, as described in Section 3.3, using object-oriented design. The GUI comprises a large widget, which consists of a number of smaller widgets, including the control widget described in Section 3.3 and an image display widget. When a CCD image is read by the GUI, it consists of 640×480 12-bit integers, each representing the intensity for a single pixel. Since Qt is limited to 8-bit displays, these integers are right-shifted by 4 bits, and the resulting values are set one-by-one in the image display widget. The CCD GUI with a star-field image in the display is shown in Figure 3.12.

3.4.1 Image Processing for the CCD Camera

The software for the camera is required to monitor the sky by recording and displaying images of it, thereby informing observers in the control room of prevailing weather conditions. Observers can visually inspect the images and check the brightness of the imaged stars, which gives an indication of relative cloud cover or poor seeing conditions. To aid observers in this task, software was developed to allow individual stars to be selected from an image and quantitative reports given on their positions and intensities. An island-finding routine was employed to locate the images of stars, followed by moment calculations and summations of pixel intensities for the user information report in the GUI.

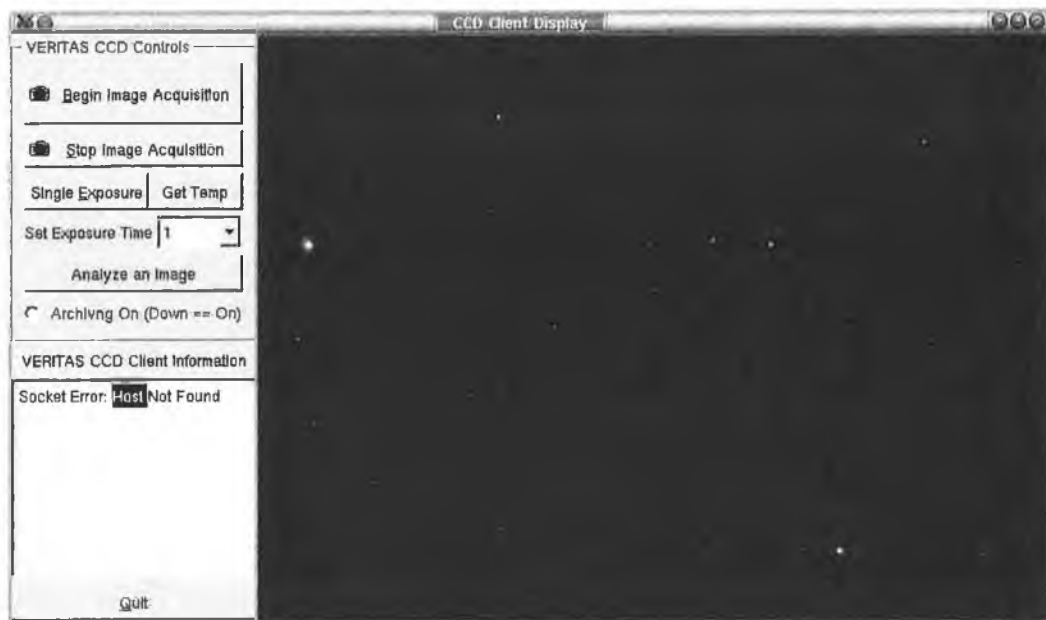


Figure 3.12: A screen-shot of the CCD GUI (the star field in the image is in the direction of the active galaxy H1426).

Image Segmentation

The process of locating the positions of stars within the CCD image is based on an island-finding algorithm, which may be outlined as follows.

Firstly, an image is taken and passed to the algorithm. The image contains 640 pixel values in width and 480 pixel values in height making a total of 307200 pixel values. Each of these pixel values is checked to see if it passes some user-defined cutoff value. If the pixel value is above this cutoff, it is considered to be part of a star image and is then passed on to the next stage, which checks neighbouring pixels for the presence of other pixels passing the cut.

A flag buffer is defined with the same number of elements as the image. The image is scanned until the first pixel passing the cut is found. A unique number is then written to the flag buffer in the same array position as the pixel that passed the cut. This now identifies that pixel as being part of a unique star. Before continuing, each neighbour pixel is checked to see if it

contains a flag. If a flag is found and it is the same as the flag number assigned to the current pixel nothing is done; however, if the flags are not the same the current flag is changed to match that of its neighbour pixel. After the whole image is scanned in this manner, a second pass is carried out to ensure that all the flags belonging to each star contain the same flag number. This second pass is necessary as, after only one pass, it can occur that several flag numbers identify different pixels in the same star. Figure 3.13 shows a numbered CCD camera pixel array with a star (represented by the red pixels) that has been imaged on it; the brighter the red, the higher the intensity of the image in that pixel. Figure 3.14 illustrates the process of

00	01	02	03	04	05	06	07
08	09	10	11	12	13	14	15
16	17	18	19	20	21	22	23
24	25	26	27	28	29	30	31
32	33	34	35	36	37	38	39
40	41	42	43	44	45	46	47

Figure 3.13: An 8×6 CCD pixel array containing an image of a star. The numbers 00 to 47 identify the individual pixels.

locating this star in software. The arrays of pixels here represent the flag buffer as defined in software, which is initially created as an array of zeros and is gradually filled with the flag numbers representing the stars in the image. The image is scanned and the first pixel passing the intensity cutoff is found at element 19 (see Figure 3.13); this is flagged with a 1. Surrounding pixels are then searched for flags (the searched pixels are represented by the hatched lines), making sure to only check the pixels that will not be included in subsequent searches (this helps to speed up the algorithm); thus pixels 10, 11, 12 and 18 are checked in this case. The process continues and the flag buffer is gradually filled with ones at positions 19, 20, 21, 28 and 29, which

correspond to the locations of the pixels containing the star image. A second pass is done to make sure that neighbouring flag numbers are all the same, but it is unnecessary in this case and nothing is changed. In this manner, the pixels belonging to the star are located and information relating it, such as the total intensity or the n^{th} order moments, can be calculated.

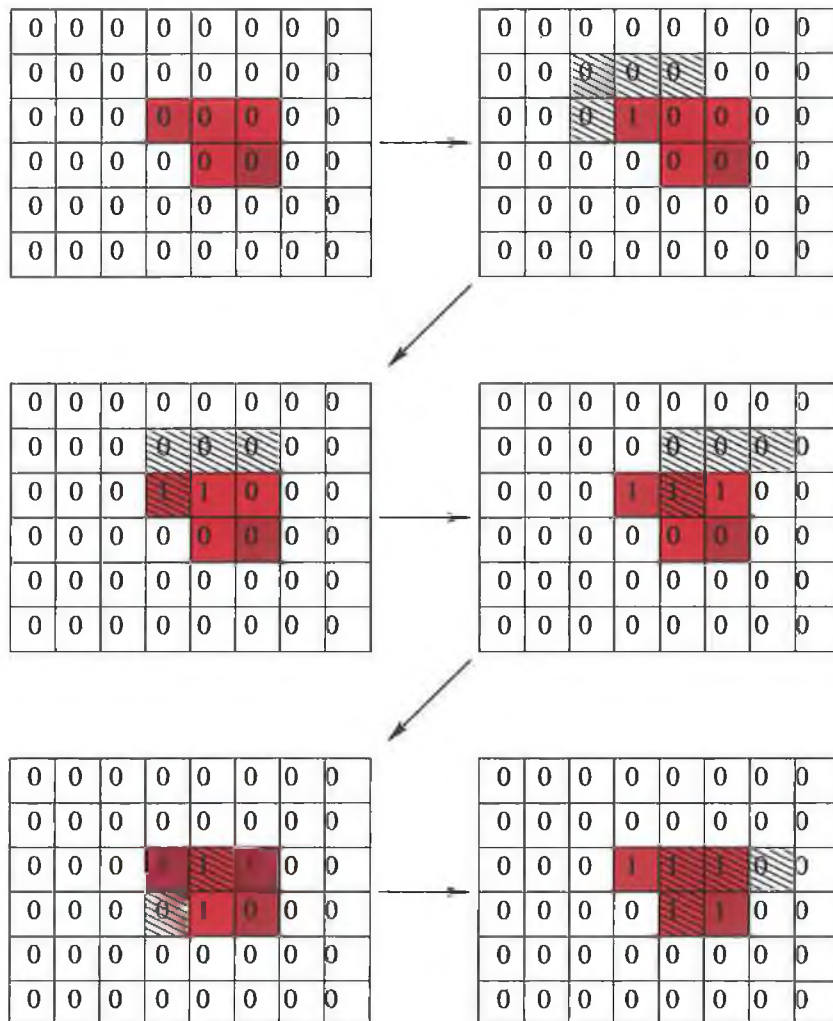


Figure 3.14: Identifying a star using the island-finding algorithm. The sequence of steps is indicated by the arrows.

Image Moments

Once the pixels which make up an individual star image have been identified, the position, shape and intensity distributions of the image can be evaluated in terms of moments, which are defined by

$$b_{kl} = \int \int x^k y^l b(x, y) dx dy, \quad (3.1)$$

where b_{kl} is one of the $k + l + 1$ moments of order $k + l$ for the object $b - b(x, y)$ represents the brightness of the object b at pixel position (x, y) in the image. The most important of these are the moments of order 0, 1 and 2.

$$\text{0th Order: } b_{00} = \int \int b(x, y) dx dy \quad (3.2)$$

$$\text{1st Order: } b_{10} = \int \int x b(x, y) dx dy \quad (3.3a)$$

$$b_{01} = \int \int y b(x, y) dx dy \quad (3.3b)$$

$$\text{2nd Order: } b_{20} = \int \int x^2 b(x, y) dx dy \quad (3.4a)$$

$$b_{02} = \int \int y^2 b(x, y) dx dy \quad (3.4b)$$

$$b_{11} = \int \int xy b(x, y) dx dy \quad (3.4c)$$

Equation 3.2 describes the moment of order 0, b_{00} , which represents the total brightness of the image. If $b_{00} \neq 1$ the image is normalised by considering $b(x, y)/b_{00}$ instead. The prototype software developed for the CCD camera uses only the zeroth and first order moments, which correspond to the image brightness and image centroid, respectively. The second order moments give a measure of the width of the star image in the x and y directions, and as such reflect the effect of a number of factors, including atmospheric conditions and telescope tracking stability.

Figure 3.15 shows a CCD image, taken with the telescope pointed at the zenith on June 6th, 2002. The result of applying the star-finding algorithm



Figure 3.15: A CCD image, taken while pointed at zenith at UT 07:48:53 on June 19th, 2002.

to this image is shown in Figure 3.16. A circle with radius proportional to the star brightness, as calculated by summing the pixel values for pixels which are part of the star image, is plotted for each star. The first order moments reveal the location of the stars relative to the centre of the camera and this defines the location of the stars in the image.

The brightness, B , of a star is related to its magnitude, m , by

$$B = k.r^{-m}, \quad (3.5)$$

where k is a proportionality constant and r is Pogson's ratio ($\sqrt[5]{100}$). Taking the logarithm to base 10 of both sides gives

$$\log_{10}(B) = \log_{10}(k) - m.\log_{10}(r) = \log_{10}(k) - 0.4m. \quad (3.6)$$

To investigate the relationship between the star magnitudes and star brightnesses in the CCD images, the brightnesses were determined (by summing pixel values) for stars of known magnitude (Table 3.1). Figure 3.17 shows a plot of $\log_{10}(B)$ versus m for these stars. The values are consistent with a straight line relationship; the substantial scatter can be attributed to differing

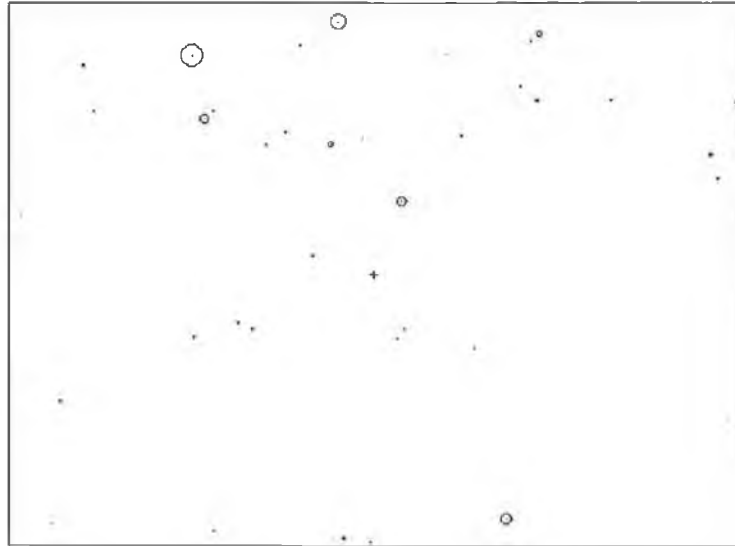


Figure 3.16: A screen-shot of the CCD GUI after applying the star-finding algorithm to the CCD image in Figure 3.15. Each star found is represented by a dot for its centre of intensity (as calculated by moment analysis) and a circle with radius proportional to the sum of its total pixel intensity.

Magnitude	Brightness
4.3	54829
5.1	41055
5.6	20871
5.7	15666
5.9	14224
6.2	17345
6.4	8143
6.6	4904
6.9	3958

Table 3.1: The magnitudes and brightnesses (determined by summing pixel values for the stars in the CCD image) of the stars used in the plot in Figure 3.17

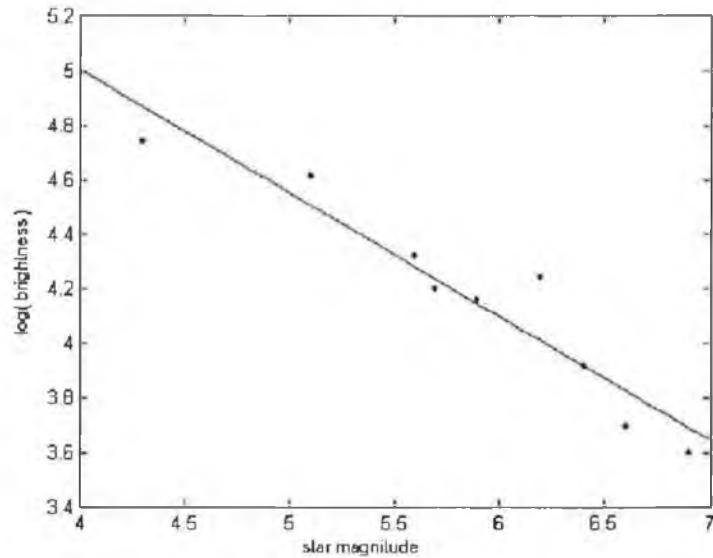


Figure 3.17: A plot of $\log(\text{brightness})$ vs. star magnitude for stars located by the star-finding algorithm in a CCD image.

stellar temperatures. The slope of the least squares fitted line is -0.45 ± 0.06 , in agreement with the expected value of -0.4 .

3.5 The FIR Pyrometer Software

A C++-based RS232 driver was written to control the FIR pyrometer. The format of the data requests to and replies from the FIR pyrometer is defined by the manufacturer, Heitronics, so the code was set up such that the correct calls to the pyrometer can be made. The emissivity setting that the pyrometer uses to estimate the temperature of the object it is looking at, can be set to values between 0.1 and 1.0 (in steps of 0.1). This is done in software by sending the `emi` command followed by the value of the setting (1.0 for the current configuration on the Whipple ten metre telescope) and the `\n` or return character (all commands must be followed by the return character). The command would therefore look as follows:

```
emi 1.0\n
```

Other settings can be changed by similar methods. The integration time used can be set to 3, for example, by sending

```
resp 3\n
```

to the RS232 interface. The ambient temperature setting can be set to read the temperature from an in-built thermometer or set manually by the user by sending `amb` followed by the relevant command. All the information sent to and returned from the pyrometer is in ASCII format, making it easy to program the code for it. When a request for the current temperature (as read by the pyrometer) is made, an ASCII string is returned and this is parsed to check for errors. If no errors are present, the string is simply the digits representing the current temperature (preceded by a minus sign if the number is negative). This string is displayed in the GUI as shown in Figure 3.18, where the temperature reading at the time the screen-shot was taken was -51.0°C . The GUI also displays the current UT time, which

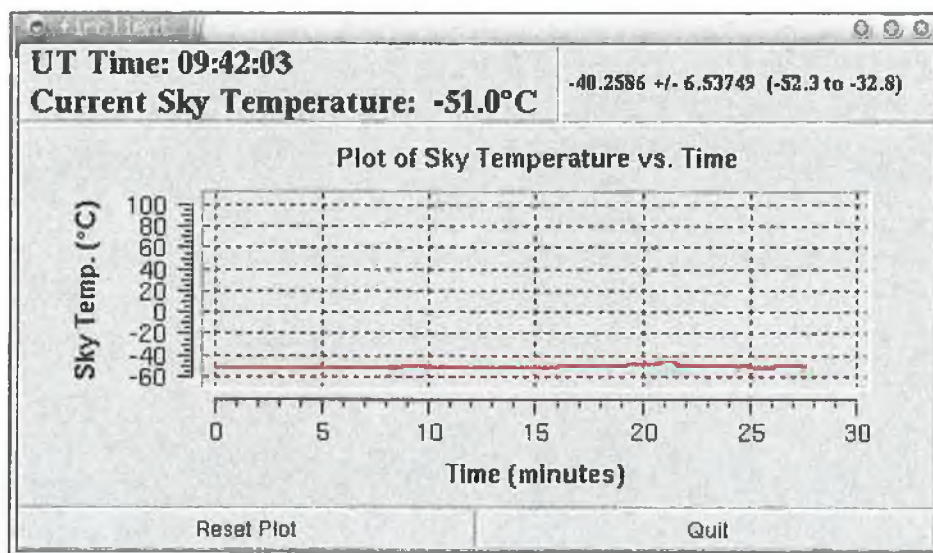


Figure 3.18: A screen-shot of the FIR pyrometer GUI.

is read from the computer clock, in the top left corner of the widget. A report on the average temperature reading and standard deviation over 30 minute periods is displayed in the top right corner; 30 minutes was chosen to

match approximately the duration of a data run taken using the telescope. A 30 minute history of the pyrometer's temperature readings is displayed as a graph of temperature versus time in the middle of the widget. This graph is generated using Qwt (<http://qwt.sourceforge.net>), which supplements Qt by providing a set of technical widgets for use in GUIs. At the end of a 30 minute display, the readings for that 30 minute period are archived (to an ASCII text file), the graph is cleared, and a new 30 minute scan commences. The archive filename, as for the CCD camera (Section 3.4), is based on the UT time and date at the time of writing. For example, data logged at UT 11:55:22 on December 11th would be stored in a file named `d12.11.11_55_22.fir`.

Chapter 4

Analysis of TeV Images from the Whipple 10m Reflector

4.1 Observing Modes

The Whipple ten metre telescope is used to detect very high energy (VHE) cosmic gamma radiation by means of the imaging atmospheric Cherenkov technique (IACT), as described in Section 1.3. Data is usually taken at the Whipple telescope in one of four modes: *on*, *off*, *tracking* and *nitrogen*. An *on* run and an *off* run are taken in succession. For the *on* run, the telescope is pointed at a specified astronomical source or potential source (whose position is identified by its right ascension and declination) and tracks this position for approximately twenty-eight minutes. As the Earth rotates, the elevation and azimuthal angles of the source change, so at the end of the *on* run, the telescope is repositioned to point to right ascension 30 minutes earlier than that of the source and the same declination as the source; this corresponds to the same elevation and azimuth as at the beginning of the *on* run (allowing 2 minutes for the telescope to slew to its new position). The new right ascension position is then tracked for 28 minutes (*off* run), covering the same elevation and azimuth path as followed by the source during the *on* run. This corrects for any systematic effects which depend on elevation or azimuth. The *off*

run can then be used to estimate the background signal that is present in the *on* run. Subsequent filtering and analysis techniques are employed to remove systematically the effects of this background signal (Section 4.2 and 4.3) from the *on* run data.

Tracking data, on the other hand, is taken by following the source for a period of time, usually either ten or twenty-eight minutes, without taking an *off* run (a *tracking* run is essentially an *on* run without a corresponding *off* run). The *tracking* mode allows the source to be followed almost continuously because several runs may be taken in succession without interruption. This mode of observation has the inherent disadvantage that there is no *off* run for estimation of the background. To overcome this, an analysis technique has been developed which estimates the background signal from the *tracking* data itself (Section 4.3).

Individual PMTs differ slightly in performance, i.e., the gain for one PMT will not necessarily be equal to that of another, even for the same model, leading to non-uniform response across the field of view of the camera. To overcome this problem, *Nitrogen* runs are used to “flat-field” the camera. The PMTs are exposed to a uniform stimulus from a pulsed nitrogen lamp positioned at the centre of the reflector. This shines the same amount of light on each PMT, so the signal recorded for each one can be used to correct for slight differences in their behaviour. Thus the relative gain of each PMT is determined for a given night and the results can then be applied to other data taken on the same night to remove the effect of any gain differences.

4.2 Image Prefiltering and Parameterisation

When the Cherenkov light image is focused on the PMTs, the signal from each PMT is transmitted to the data acquisition system. The signals from each of the inner tubes (see Section 1.4) are first fed to a set of amplifiers (one amplifier for each tube) and a set of discriminators is used to check whether or not the event should be recorded for subsequent data analysis.

The output from each amplifier is split: one portion of the signal is delayed, while the other is fed to a constant fraction discriminator. The constant fraction discriminators are used to determine whether a channel has fired. The discriminators take the direct amplified PMT signal as their input, and output a pulse of preset amplitude and duration when the signal rises above some threshold. A multiplicity trigger checks to see if the signals from at least three tubes are above some preset threshold (typically 35mV) and a pattern selection trigger (PST) ensures that the event is recorded only if at least three of these tubes are adjacent (Bradbury 1997). If the signals pass these criteria, an electronic “gate” is opened, and the delayed signals are fanned out to ADCs and recorded.

As described in Moriarty et al. (1997), there are many factors which contribute to the appearance, shape and size (light content) of each image as recorded by an imaging camera. Factors relating to the camera and the telescope include the point of impact of the shower on the ground relative to the telescope, the optical quality and focusing characteristic of the mirror(s), noise in the photomultiplier tubes and signal processing electronics, signal integration time constants, and finite charge pedestals associated with individual ADC channels. External factors, independent of the telescope, include the nature and energy of the primary particle, geomagnetic influences on the development of individual showers, the elevation of the source during observations, the presence of bright stars in the direction of the source, the presence of background light or air-glow and the sky transparency at the time of observation.

Artificially triggered events interspersed in the Cherenkov image data are used to determine the “pedestals” (these are the ADC values in the absence of Cherenkov light) and the mean pedestal values are subtracted from each image. The pedestals are deliberately set at small positive values to allow sky noise fluctuations to be recorded. Difference in sky brightnesses between *on* and *off* sky regions (see Section 4.1) can introduce biases, which may be severe for events close to the threshold. The method used to address this

problem is to equalise the noise levels between the *on* and the *off* regions using simulated Gaussian noise, a process referred to as “software padding” (Cawley 1993). Following these preliminary steps, images are cleaned using the “picture/boundary” method (Punch et al. 1991). Any tube which has a signal greater than 4.25 times the pedestal variance for that tube is considered to be in the “picture”; any tube which has a signal greater than 2.25 times its pedestal variance and which is adjacent to a picture tube is considered to be in the “boundary”. All other tubes, dominated by sky noise, are treated as having zero signal.

The aim of high-resolution imaging systems is to exploit attributes of individual captured images, in order to maximise the rejection of background events, while minimising the erroneous rejection of genuine gamma-ray events. The ideal of 100% background rejection and 100% gamma-efficiency is not attainable in practice, due to similarities in the development of electromagnetic and hadronic cascades, which make complete separation of the resultant Cherenkov images impossible. Monte Carlo simulations of shower development and of the detection characteristics of Cherenkov telescopes (Kertzman & Sembroski 1994) have played a significant role in the development of successful gamma/hadron discrimination techniques. These simulations predict that images of gamma-ray showers are compact and essentially elliptical in shape.

4.3 The Atmospheric Cherenkov Imaging Technique

As mentioned in Section 1.3, gamma-ray events are far less numerous than background hadronic cosmic-ray induced events. Fortunately, in addition to preserving directional information contained in an electromagnetic air shower (EAS), the Cherenkov image formed on the camera pixels also contains important information pertaining to the nature of the primary particle. With the telescope pointing at a VHE gamma-ray source, the image resulting from

a typical gamma-ray induced shower is compact and elliptical, and has an orientation that points toward the centre of the camera. Images resulting from hadronic cosmic rays, however, are far more irregular in shape and are randomly oriented in the focal plane. Figure 4.1 shows typical images resulting from gamma-ray induced (left) and hadron-induced (right) showers. Figure

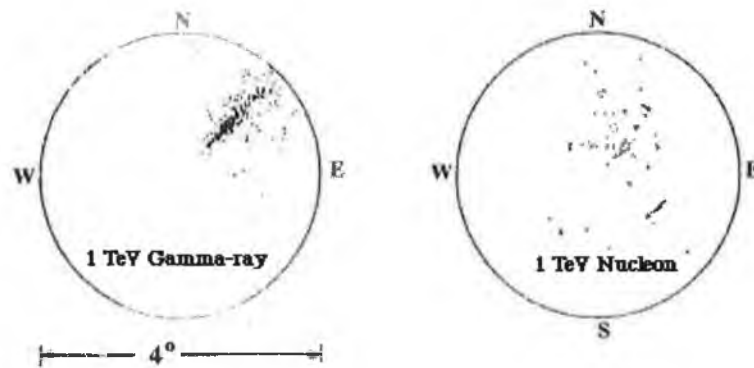


Figure 4.1: A gamma-ray induced image (left) and a hadron-induced image at the focal plane of an imaging Cherenkov telescope (right)

4.2 shows the typical development of both types of shower. The hadron-induced shower tends to be broader and longer than that of the gamma-ray shower. This is due to the fact that particles produced in the first few collisions in cosmic-ray showers contain significantly more transverse momentum than their gamma-ray equivalents and because the nucleonic component of the cosmic-ray shower penetrates deeper into the atmosphere. When the Cherenkov light from an EAS is imaged on a Cherenkov telescope's array of PMTs, an ellipse can be fitted to it in order to characterise the distribution of the light. A gamma-ray shower will produce a compact ellipse (see Figure 4.3), whereas a cosmic-ray shower will produce a larger one.

To characterise the images, a set of parameters known as the "Hillas parameters" was developed (Hillas 1985). The parameters themselves are discussed in Section 4.3.1. These parameters are calculated for each image (see Appendix A), assuming the image is elliptical, and lower and upper bounds on each parameter can be used to select events for classification as

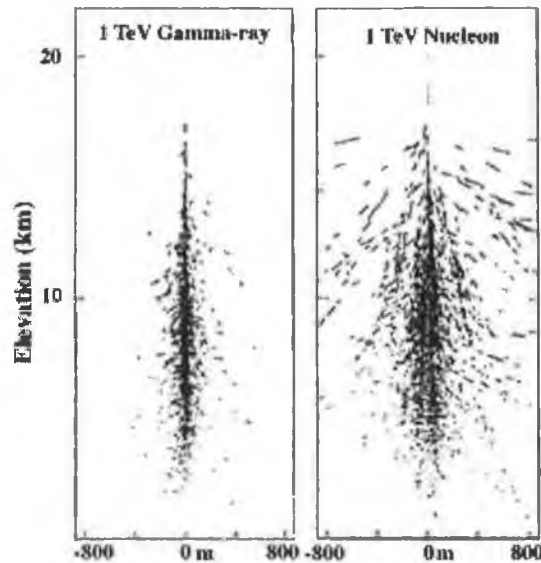


Figure 4.2: A gamma-ray initiated air shower (left) and a hadron-initiated air shower (right)

“gamma-ray” events. Only images satisfying each of the parameter bounds are classified as gamma rays. This method of gamma-ray/hadron discrimination is known as “Supercuts” (Reynolds et al. 1993) and is the preferred method of the Whipple collaboration, used in their detection of numerous sources. With the application of Supercuts, the Whipple system is capable of rejecting 99.7% of the background events, while keeping $\sim 50\%$ of the gamma-ray events.

4.3.1 Hillas Parameters

For each image taken by the telescope, six parameters are calculated to characterise its shape and orientation (Figure 4.4). These are: *Width*, *Length*, *Miss*, *Distance*, *Azwidth*, and *Alpha*.

- *Width*: The rms spread of the light along the minor axis of the image ellipse. This gives a measure of the lateral development of the shower.
- *Length*: The rms spread of the light along the major axis of the image

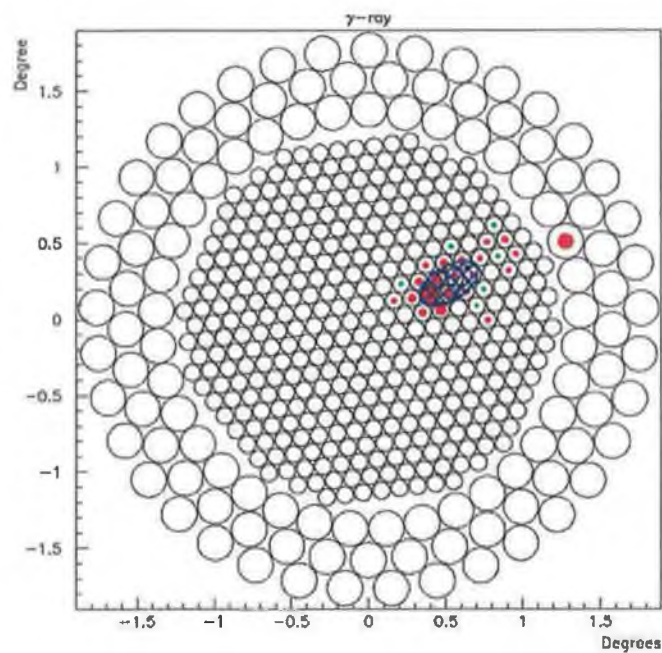


Figure 4.3: A gamma-ray event imaged on an array of PMTs with an ellipse fitted to it to characterise its shape. The size of the circle represents the tube intensity. Red tubes are "picture" tubes and green tubes are "boundary" tubes.

ellipse. This gives a measure of the vertical development of the shower.

- *Miss*: The perpendicular distance between the major axis of the image ellipse and the centre of the field of view. This gives a measure of the shower orientation.
- *Distance*: The distance from the centroid of the image ellipse to the centre of the field of view. This gives a measure of the separation between the shower axis and the optic axis.
- *Azwidth*: The rms spread of light perpendicular to the line connecting the centroid of the image ellipse to the centre of the field of view. This gives a measure of both the size and orientation of the image ellipse.
- *Alpha*: The angle between the major axis of the image ellipse and the line joining the centroid of the ellipse to the centre of the field of view. It is calculated from $Alpha = \sin^{-1}(Miss/Distance)$.

Two additional parameters, *Size* and *Frac3*, are used in the analysis.

- *Size*: The measure of the total light contained in the image after cleaning, expressed in digital counts (d.c.). This gives an indication of the energy of the primary particle.
- *Frac3*: The fraction of the total digital count contained in the three highest tubes. This is used to reject spurious events such as those caused by charged particles (typically muons) physically passing through PMTs in the camera.

4.3.2 Rate and Significance

Once the data have been parameterised and the parameter cuts applied, an excess of gamma rays may be left if the source is emitting them at the time of observation. Two different methods of quantifying the result of this are then employed, depending on the observing mode used (i.e., *on/off* or *tracking*).

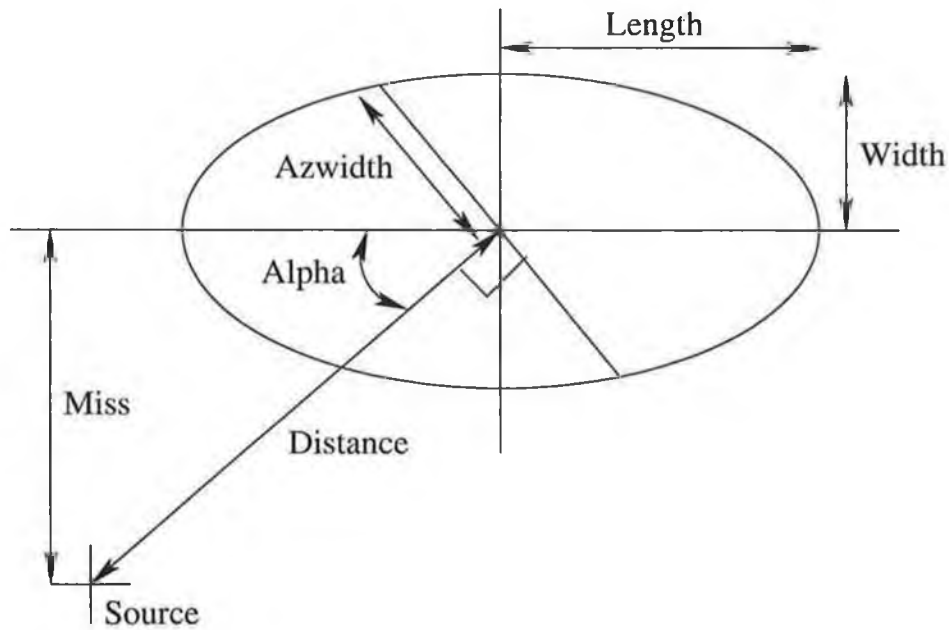


Figure 4.4: Diagram illustrating the Hillas parameters.

On/Off Analysis

In *on/off* analysis the rate, r , in gamma rays per minute and the uncertainty associated with it, Δr , are calculated from:

$$r \pm \Delta r = \frac{ON - OFF}{t} \pm \frac{\sqrt{ON + OFF}}{t}, \quad (4.1)$$

where ON and OFF are the number of events that pass the cuts in the *on* and *off* runs respectively and t is the observation time in minutes. The statistical significance of this result, in terms of standard deviations above the mean background level, σ , is then calculated from

$$\sigma = \frac{r}{\Delta r} = \frac{ON - OFF}{\sqrt{ON + OFF}}. \quad (4.2)$$

The actual parameter cuts are derived by optimising the significance obtained when the cuts are applied to a known source of VHE gamma rays. For work in the northern hemisphere, the Crab Nebula is considered a “standard candle” for this purpose. For the 2001–2002 observing season (September 2001 to July 2002), the standard set of cuts derived are shown in Table 4.1.

A useful indication of whether there is an excess of gamma-ray events from the direction of a source can be obtained by superimposing the *Alpha* distributions for the *on* and *off* data.

Parameter	Range
<i>Width</i>	0.05°–0.12°
<i>Length</i>	0.13°–0.25°
<i>Distance</i>	0.40°–1.00°
<i>Alpha</i>	0°–15°
<i>Length/Size</i>	4×10^{-4} (°/d.c.)
<i>Frac3</i>	0.98

Table 4.1: The standard set of parameter cuts used by the Whipple Collaboration for data taken during the 2001–2002 observing season.

Figure 4.5 shows a plot of *Alpha* distributions for *on* and *off* data taken in the direction of the Crab Nebula. All the cuts except for the *Alpha* cut have already been applied and this plot shows how the number of events in each *Alpha* value bin varies from 0° to 90°. A clear excess in the region 0°–20° can be seen in the *on* data, which is as expected if there is a gamma-ray source at the centre of the camera’s field of view. The *off* data are more or less isotropic, and the *on* data matches it well beyond 20°. In the *on* data there are 554860 events, only 2547 of which pass *both* the shape and orientation cuts. The *off* data contains 552984 events, of which only 1675 events pass these same cuts. The two data sets were taken over equal durations of 303.21 minutes, so

$$r \pm \Delta r = \frac{2547 - 1675}{303.21} \pm \frac{\sqrt{2547 + 1675}}{303.21}. \quad (4.3)$$

This gives a rate of 2.876 ± 0.214 gammas per minute and a statistical significance $\sigma = 13.42$ standard deviations.

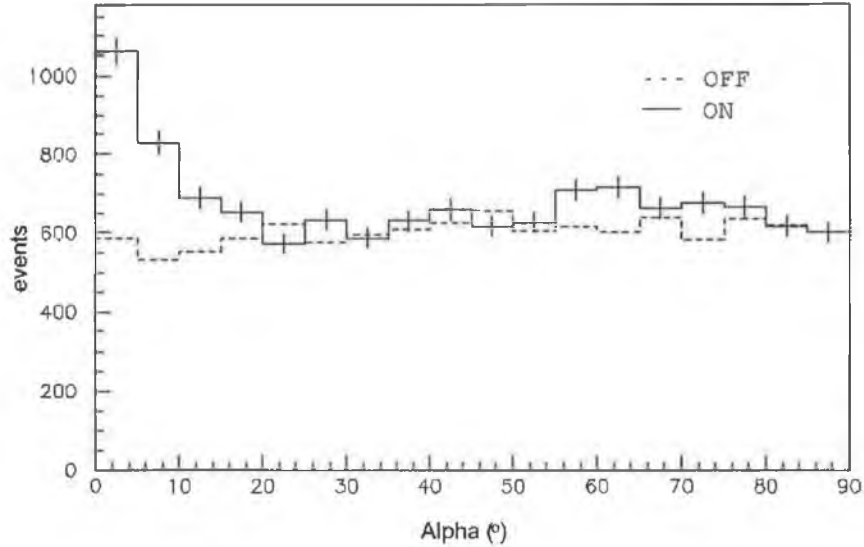


Figure 4.5: Plot of the *Alpha* distribution of events passing the shape cuts for *on* and *off* data taken in the direction of the Crab Nebula.

Tracking Analysis

In *tracking* analysis, there is no control region with which to compare the *tracking* run, so the background must be estimated using the *on* source data itself. The technique employed uses the distribution of the *Alpha* parameter after all the shape-based cuts such as *Width*, *Length*, *Distance* and *Size* have been applied. In *on* and *off* data that have passed the shape cuts, *Alpha* values beyond 20° are closely matched, as illustrated in the data plotted in Figure 4.5, while the excess in the *on* run is concentrated below 15° . By taking the ratio of counts in the region 0° – 15° to counts in the region 20° – 65° for the *off* run a number known as the “tracking ratio” (denoted β) can be calculated. For a perfectly flat distribution, this should give $\beta = \frac{1}{3}$, but in practice the value may differ from this due to systematic effects such as sky brightness, or stars in the field of view. This number can then be applied to the *Alpha* distribution in the region 20° – 65° of the *tracking* data to calculate the expected background counts in the 0° – 15° region. This assumes that the

shape of the *Alpha* distribution is consistent for a given sky region, which is generally found to be the case.

To get the tracking ratio, *off* data is still required, but not necessarily *off* data corresponding to a specific *on* run. The tracking ratio is calculated from

$$\beta \pm \Delta\beta = \frac{C_{ON}}{C_{OFF}} \pm \sqrt{\frac{C_{ON}}{C_{OFF}^2} + \frac{C_{ON}^2}{C_{OFF}^3}}, \quad (4.4)$$

where C_{ON} is the number of counts in the 0° – 15° range of the *Alpha* distribution and C_{OFF} is the number of counts in the 20° – 65° range. C_{ON} and C_{OFF} can come from a large *off* data set, which reduces the statistical uncertainty associated with β .

The rate, r , and the uncertainty associated with it, Δr , can then be calculated from

$$r \pm \Delta r = \frac{ON - \beta OFF}{t} \pm \frac{\sqrt{ON + \beta^2 OFF + \Delta\beta^2 OFF^2}}{t}, \quad (4.5)$$

where ON is now the number of events in the 0° – 15° region, and OFF the number of events in the 20° – 65° region, which is scaled by the tracking ratio, β . The statistical significance, σ , is determined as

$$\sigma = \frac{r}{\Delta r} = \frac{ON - \beta OFF}{\sqrt{ON + \beta^2 OFF + \Delta\beta^2 OFF^2}}. \quad (4.6)$$

Figure 4.6 shows the *Alpha* distribution for *tracking* data taken on Markarian 421 during January 1998. The raw data consists of 807748 events taken over 1062.75 minutes of observation. 2642 of the events that passed the shape cuts lie in the *ON* region (0° – 15°) of the *Alpha* distribution and 5588 lie in the *OFF* region (20° – 65°) of the *Alpha* distribution. Using a tracking ratio of $\beta = 0.345 \pm 0.005$ (determined using Equation 4.4 from a large sample of *off* run data) the rate can be calculated as

$$r \pm \Delta r = \frac{2642 - 0.345 \times 5588}{1062.75} \pm \frac{\sqrt{2642 + 0.345^2 \times 5588 + 0.005^2 \times 5588^2}}{1062.75}, \quad (4.7)$$

which gives a rate of 0.67 ± 0.06 gammas per minute and a statistical significance $\sigma = 11.2$ standard deviations. The parameter cuts applied were

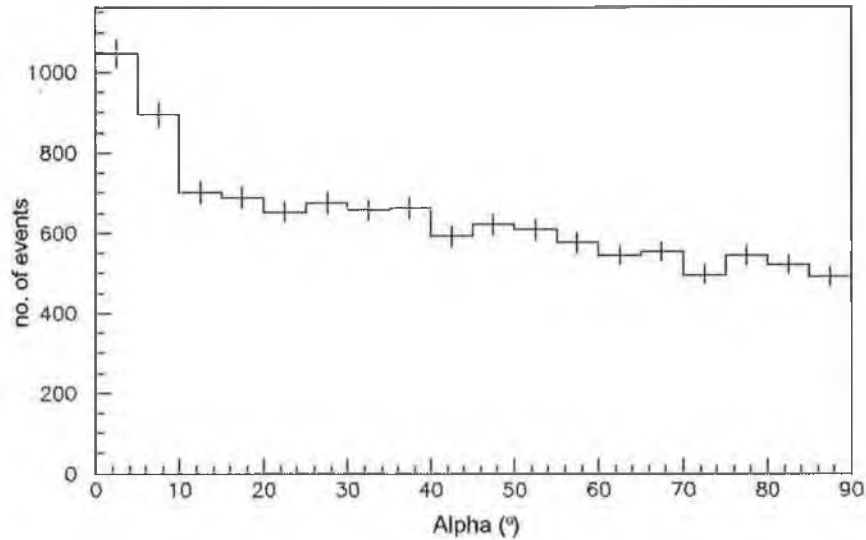


Figure 4.6: Plot of the *Alpha* distribution for events passing the shape cuts for *tracking* data taken on Markarian 421 in January 1998.

the standard set of Supercuts derived for data taken in 1997, during the 1996–1997 season, shown in Table 4.2.

Parameter	Range
<i>Width</i>	0.07°–0.16°
<i>Length</i>	0.16°–0.33°
<i>Distance</i>	0.51°–1.17°
<i>Alpha</i>	0°–15°
<i>Length/Size</i>	1 (°/d.c.)
<i>Frac3</i>	0.98

Table 4.2: The standard set of parameter cuts used by the Whipple collaboration for data taken in 1997, during the 1996–1997 observing season.

Chapter 5

Detection of TeV Gamma-Ray Emission from the BL Lacertae Object 1ES1959+650

5.1 Introduction

Many different types of galaxy exist throughout the universe. A small percentage of galaxies display an extremely bright central nucleus, which outshines the billions of stars that make up the rest of the galaxy. Because of the overall star-like appearance, the term “quasi-stellar object” (QSO), shortened to quasar, was used to describe such entities. These objects are now categorised into sub-classes and the generic type is referred to as an “active galactic nucleus” or AGN.

Among the most extreme members of the AGN family are BL Lacertae objects (BL Lacs). This type of AGN is named after its first known example, BL Lacertae, which was originally classified (incorrectly) as a variable star. BL Lacs are grouped together with flat-spectrum radio quasars (FSRQs) to form a class of object known as “blazars”, characterised by extremely variable, non-thermal spectral energy distributions (SEDs). One property which differentiates blazars from most other AGN is the complete lack of

discrete emission lines in their spectra. Blazar emission extends from radio to gamma-ray frequencies and is believed to be produced in a highly relativistic plasma jet closely oriented with the line of sight to the Galaxy (Urry & Padovani 1995; Blandford & Rees 1978). Figure 5.1 shows a ground-based telescope image of the active galaxy NGC4261 (left) and a Hubble Space Telescope image of the central region of the galaxy (right). The images indicate the presence of relativistic particle jets emerging from the central core, believed to harbour a super-massive black hole.

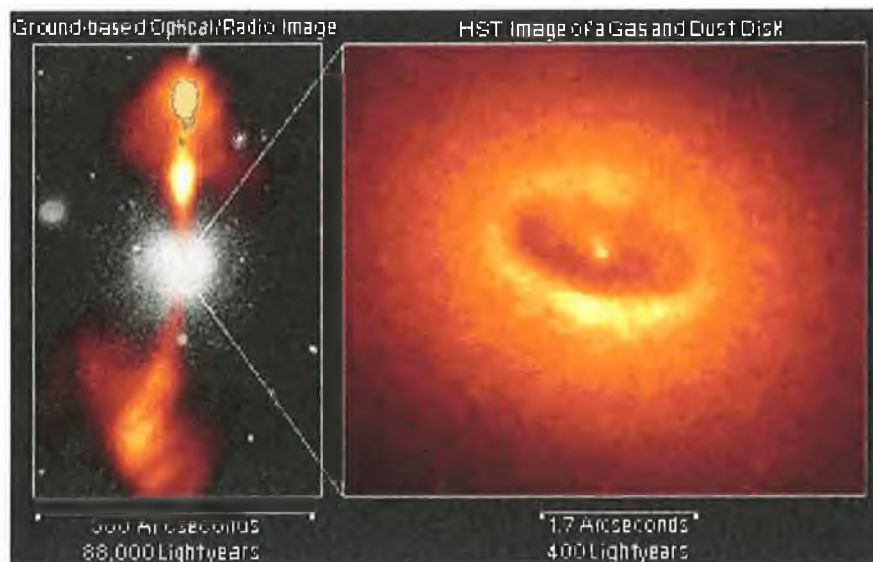


Figure 5.1: Ground-based and Hubble Space Telescope images of the active galaxy NGC4261.

The SEDs of BL Lacs typically show two peaks; the lower energy peak is usually attributed to synchrotron radiation from relativistic electrons and the higher energy peak is thought to be due to inverse Compton scattering by these same electrons. Alternative explanations for the high-energy component invoke pair cascades triggered via pion and pair photo-production from high-energy protons in the jet (Mannheim 1993) or proton synchrotron radiation (Aharonian 2000; Mücke & Protheroe 2001). Figure 5.2 shows the spectral energy distributions, expressed as power per logarithmic band-

width, for the active galaxies Markarian 421 (Mrk 421) and Markarian 501 (Mrk 501). The data were derived from contemporaneous multi-wavelength observations and an average of non-contemporaneous archival measurements (Buckley et al. 1997; Kataoka et al. 1999; Catanese et al. 1997b; Catanese & the Whipple Collaboration 1999). Both plots have a synchrotron peak at X-ray frequencies, characteristic of X-ray selected BL Lac type AGN, and a high-energy peak whose precise location is uncertain, but which must lie in the 10–250GeV region, between EGRET (see Section 1.3) and imaging atmospheric Cherenkov telescope (IACT) observations. The synchrotron and high-energy peaks are similar in power output.

BL Lacs also possess extreme variability on time scales from minutes to years. Large variability within these short times places strong constraints on the size of the emission region. The first clear detection of flaring activity in the VHE emission of an AGN came in 1994 observations of Markarian 421 by the Whipple Collaboration (Kerrick et al. 1995) where a 10-fold increase in the flux was observed, from an average level that year of approximately 15% of the Crab Nebula flux to approximately 150% of the Crab Nebula flux.

Many BL Lacs have been detected at GeV energies (Mukherjee et al. 1997). The EGRET catalogue includes in excess of 66 blazars above 100MeV (Hartman et al. 1999). For ground-based Cherenkov telescopes operating above ~ 300 GeV, however, only a handful have been so far detected. Markarian 421 with redshift $z = 0.031$ (Punch et al. 1992) and Markarian 501 with redshift $z = 0.034$ (Quinn et al. 1996) are now strongly confirmed sources, seen by more than one ground-based atmospheric Cherenkov telescope at or above the 5σ level. 1ES2344+514 ($z = 0.044$) (Catanese et al. 1998) and PKS2155-304 ($z = 0.116$) (Chadwick et al. 1999) are two less conclusive sources, having been detected only once. This evidence may indicate that low-redshift, X-ray selected BL Lac objects (XBLs) may be the only extragalactic gamma-ray sources observable at TeV energies. However, note that H1426+428 with $z = 0.129$ has recently been reported as a source by the Whipple Collaboration (Horan et al. 2002) and by the HEGRA collaboration

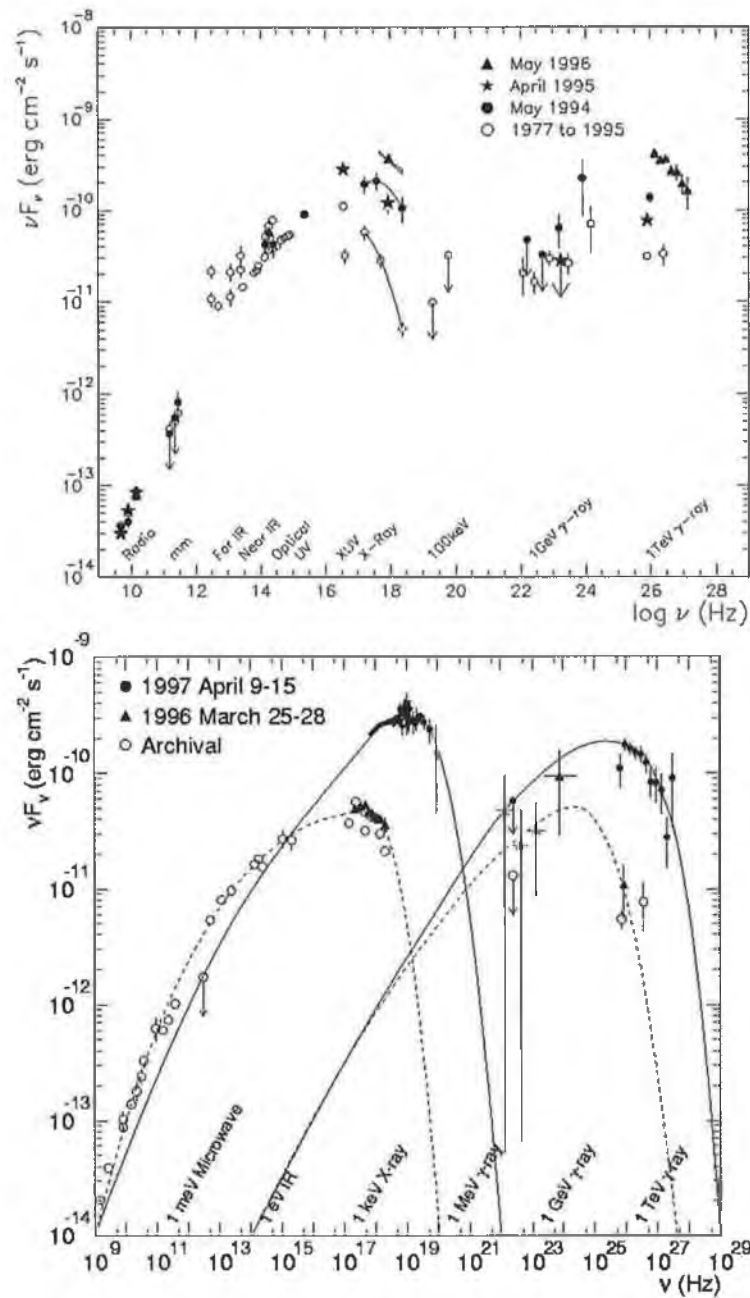


Figure 5.2: The spectral energy distribution of Mrk 421 (top) and Mrk 501 (bottom) from contemporaneous and archival observations (Buckley et al. 1997; Kataoka et al. 1999; Catanese et al. 1997b; Catanese & the Whipple Collaboration 1999). The curves are meant to guide the eye to contemporaneously measured points and do not represent fits to the data

(Aharonian et al. 2002), albeit at a very low flux. All of these objects can be classified as high-frequency peak BL Lacs (HBLs) (Padovani & Giommi 1995) based on the location of the lower energy peak in their SEDs.

5.2 Motivation for Observations on 1ES1959+650

The AGN 1ES1959+650, at $z = 0.048$, is not a particularly extreme example of a HBL, but observations on it suggested that it might be a TeV emitter based on its SED, which has a relatively high lower-energy peak. Measurements with the X-ray satellite *BeppoSAX* in 1997 (Boella et al. 1997) placed the lower energy peak in the SED at 4eV (Beckmann 2002). This is to be compared with $\sim 1\text{keV}$ for Markarian 421 (Maraschi et al. 1999) and $\sim 100\text{keV}$ for Markarian 501 during its 1997 flare state (Pian 1998), although for both of these sources the position of the peak is known to vary widely depending on the flux level. 1ES1959+650 is present in the third EGRET catalogue with an average measured flux of $1.8 \times 10^{-7}\text{photons.cm}^{-2}.\text{s}^{-1}$ for energies less than 100MeV (Hartman et al. 1999) and has been predicted to have the third highest flux (after Markarian 421 and Markarian 501) above 300GeV, based on simple scaling arguments (Stecker et al. 1996). Costamante & Ghisellini (2002) have also predicted it to be a TeV emitter

According to the detection criteria suggested by Weekes (1999), previous observations of the object have been inconclusive. A detection with statistical significance of 3.9σ was reported by the Utah 7 Telescope Array (Nishiyama et al. 1999) based on 57 hours of observation. The telescope array operated by the HEGRA Collaboration at La Palma in the Canary Islands, recently reported a preliminary detection at $\sim 5\sigma$ with over 100 hours of data (Konopelko 2002). Previous observations of 1ES1959+650 with the Whipple ten metre telescope produced only an upper limit at a flux level of $1.3 \times 10^{-11}\text{photons.cm}^{-2}.\text{s}^{-1}$ (Catanese et al. 1997a). However, during the period of May–July 2002, a clear detection of TeV emission was made (Dow-

dall et al. 2002; Holder et al. 2003) and rapidly confirmed by the HEGRA Collaboration (Horns & Konopelko 2002).

5.3 TeV Emission from 1ES1959+650

1ES1959+650 is optimally observed in the period around July each year, this being the time of year when it is highest in the sky as seen from the Whipple Observatory. Observations at the Whipple ten metre telescope are curtailed from July until September each year because of adverse weather conditions, including lightning storms that can cause serious damage to the telescope system. Data on 1ES1959+650 are therefore only taken there during May–June or September–October. For observations from Mount Hopkins (latitude $31^{\circ}57.6'N$), 1ES1959+650 culminates at zenith angle $\theta_Z = 33.5^{\circ}$, so all the data were taken at large zenith angle ($33.5^{\circ} < \theta_Z < 53.5^{\circ}$). In mid-May 2002, a short exploratory scan of the source was taken, as it had just risen to a sufficient elevation for observations. On May 16th, with the source at an elevation of 55° , a twenty-six minute tracking run was taken at the end of the night's observing, just before astronomical twilight when observations must stop because of imminent sunrise. This scan produced a signal with a rate of 1.75 ± 0.53 gamma-ray events per minute, corresponding to a significance of 3.29σ . Although this is not a particularly high significance, it was an indication of a possible detection and suggested that longer, more comprehensive scans might give more information. As soon as was possible on May 17th, a more intense campaign of *on/off* observation was begun. At the beginning of the night's observing, the source was at an elevation of only 36° , but showed a rate of 3.46 gamma per minute with a significance of 5.53σ . During the course of observations, as the source rose in the sky, the rates and significances climbed higher with each data run. Table 5.1 summarises the results obtained from tracking analysis of these data using the methodology described in Chapter 4 and the cuts shown in Table 4.1.

Observations of 1ES1959+650 were continued on moonless nights for the

MJD -2452000	UT Start Time	Elevation/ $^{\circ}$	Rate gamma/minute	Significance/ σ
410.5	10:40	55	1.75	3.29
411.5	06:58	36	3.46	5.53
411.5	07:57	42	3.26	5.44
411.5	09:00	48	3.46	6.46
411.5	10:00	52	4.77	8.36
411.5	10:58	55	8.14	7.04

Table 5.1: Rates, significances and elevations for first two days of the detection of 1ES1959+650 at the Whipple Observatory.

remainder of May and during the month of June. The total dataset accumulated consists of 38.75 hours of on-source data and 6.47 hours of off-source data. A plot of the average gamma-ray rate per day, calculated from tracking analysis of the data, is shown in Figure 5.3. It is evident that gamma-ray emission from this source is highly variable on this time scale. From June 3rd

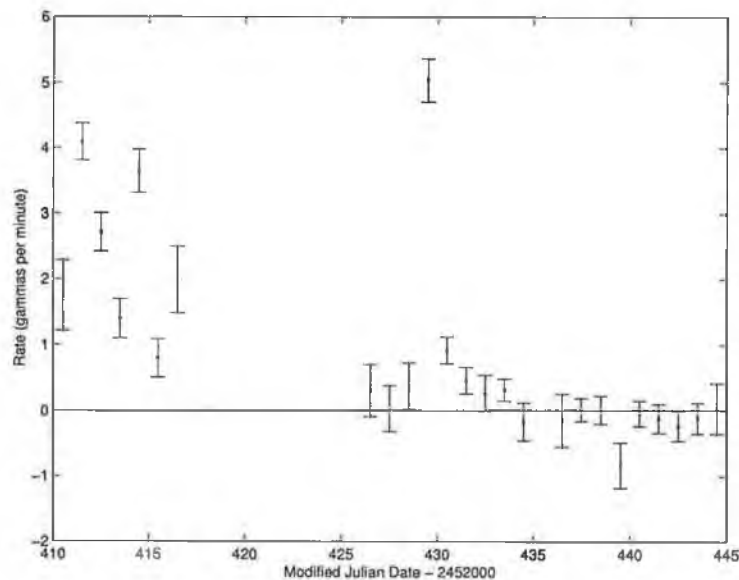


Figure 5.3: Plot of average daily rates for data taken on 1ES1959+650 in May and June 2002.

to June 4th (MJD 2452432–2452433), the average gamma-ray rate rose from

0.38 ± 0.35 gamma/minute to 5.04 ± 0.33 gamma/minute, then fell back to 0.92 ± 0.20 on June 5th. This corresponds to a doubling time of ~ 6.5 hours, calculated from

$$t_{double} = \frac{t_1 - t_2}{\log_2(r_1/r_2)}, \quad (5.1)$$

where $t_1 - t_2$ is the time interval between the two observation times (~ 24 hours) and r_1 and r_2 are the average rates on these days. While this is not as short as the most extreme case observed for Mrk 421 in 1996 (Gaidos et al. 1996), when the rate was seen to double on a time scale of 15 minutes, it is nevertheless indicative of a very small emission region at the source.

On/off analysis of the the 14 *on/off* pairs taken during May and June 2002 reveals an average rate of 2.59 ± 0.15 gamma/minute, which is statistically significant at 16.2σ above the mean background. *Tracking* analysis performed on all the on-source data taken during May and June 2002 gives an average rate of 1.02 ± 0.06 gamma/minute, which is statistically significant at a level of 17σ . *Alpha* plots for both the *on/off* and *tracking* data are shown in Figure 5.4 and Figure 5.5 respectively.

This represents the first unequivocal detection of 1ES1959+650 as a source of TeV gamma radiation, making it only the third AGN detected with such high significance at TeV energies.

5.4 Variability Analysis

BL Lacs show extreme variability, which is believed to be related to processes occurring within their relativistic jets. In order to check if the gamma-ray rate during a specified period (e.g., a month) is constant about the mean for that period, a chi-squared (χ^2) test is performed. If O_k is the observed rate for a given day in a month and E_k the expected rate for that day (i.e., the mean rate for that month), then the χ^2 value is calculated as

$$\chi^2 = \sum_{k=1}^n \frac{(O_k - E_k)^2}{E_k}. \quad (5.2)$$

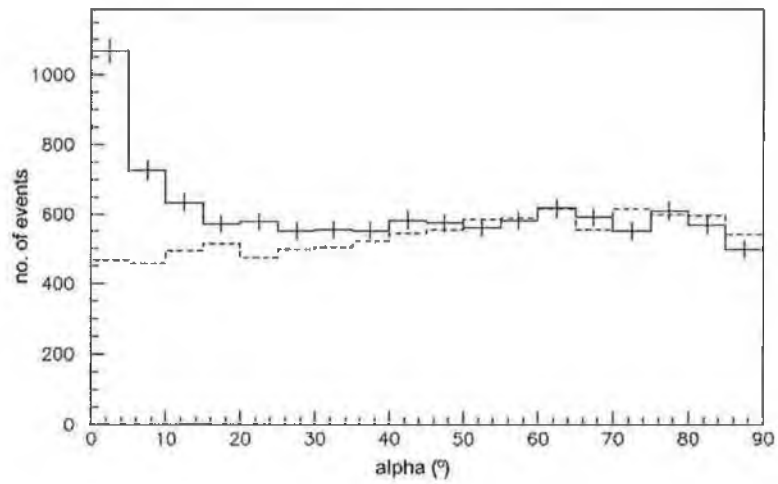


Figure 5.4: *Alpha* plot for *on/off* analysis of 1ES1959+650 data (May–June 2002)

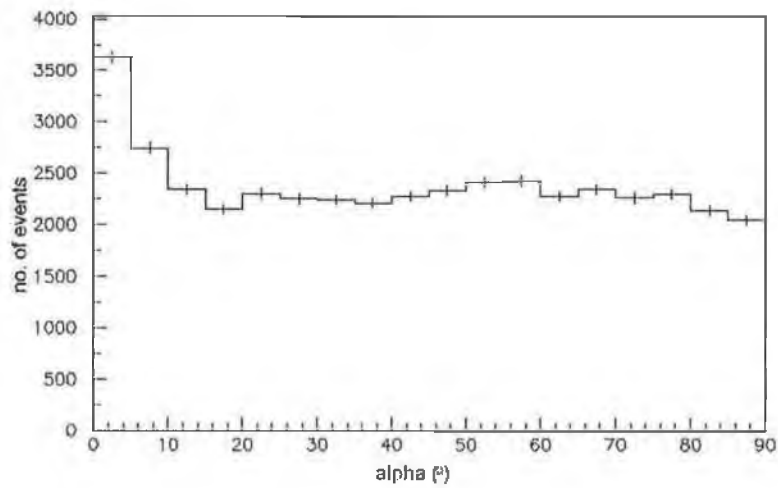


Figure 5.5: *Alpha* plot for *tracking* analysis of 1ES1959+650 data (May–June 2002)

If there are n measurements E_k , with standard deviation σ_k , χ^2 is calculated as

$$\chi^2 = \sum_{k=1}^n \left(\frac{O_k - E_k}{\sigma_k} \right)^2. \quad (5.3)$$

The value of χ^2 is an indicator of the agreement between the observed and expected numbers. If $\chi^2 = 0$, the agreement is perfect and $O_k = E_k$ for all values considered. In general, with n values considered, if $\chi^2 \leq n$ it can be concluded that the data are distributed as expected. Conversely, if $\chi^2 \gg n$ the observed and expected values differ significantly and it can be concluded that the data are not governed by the expected distribution.

Once the χ^2 test is performed it may be desirable to find the probability of the calculated χ^2 value occurring by chance, taking into account the size of the sample and the number of variables (degrees of freedom). This can be done by consulting a table containing probabilities for χ^2 , calculated from a standard integral, or in software by calculating the integral using gamma functions.

When the 1ES1959+650 data taken during the month of May were subjected to this χ^2 analysis, the result indicated that there is a probability of 1.76×10^{-31} that the observed rates could occur by chance if the rate was actually constant at the average rate for the month. The χ^2 test for June reveals a similarly low χ^2 probability of 2.42×10^{-67} . This confirms the strong intra-month variability of the source visually apparent in Figure 5.3.

A test for variability on time scales of less than one day is less conclusive. On May 17th, the rates for 5 consecutive runs were 3.46, 3.26, 3.46, 4.77 and 8.14 gammas per minute, respectively, giving a χ^2 probability of 2.35×10^{-4} for chance occurrence. Similar analysis gives probabilities of 0.29 for May 18th, 0.30 for May 19th and 0.52 for May 20th, indicating that the distributions on those nights are consistent with a constant rate. A histogram of χ^2 probabilities for individual observing days during May 2002 and June 2002 is shown in Figure 5.6 and the probabilities themselves are plotted in Figure 5.7. The histogram indicates that there is no evidence for variability of the source on this time scale. This is in sharp contrast to data taken on

Mrk 501, where the histogram of χ^2 values to check for intra-night variability shows a distinct peak for probabilities lower than 0.025 (Quinn et al. 1999). These results imply significant hour-scale variability for Mrk 501; however, in the case of 1ES1959+650, strong variability on time scales of less than one day does not appear to be present.

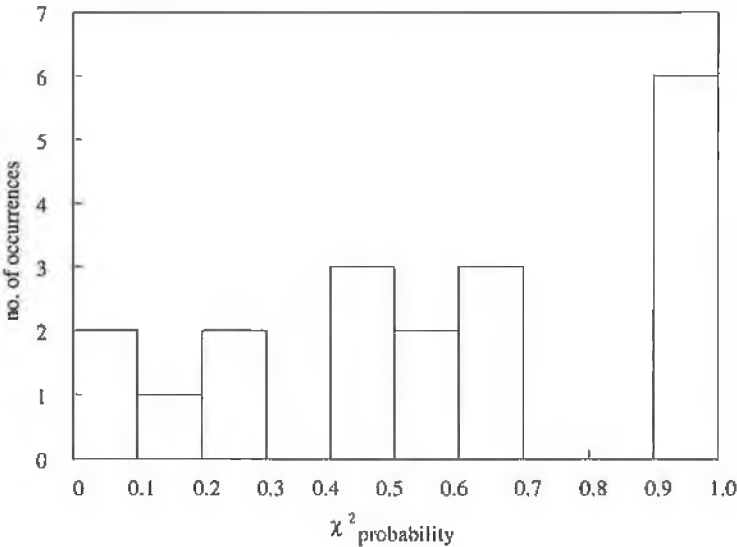


Figure 5.6: A histogram of χ^2 probabilities for observing days during May and June 2002.

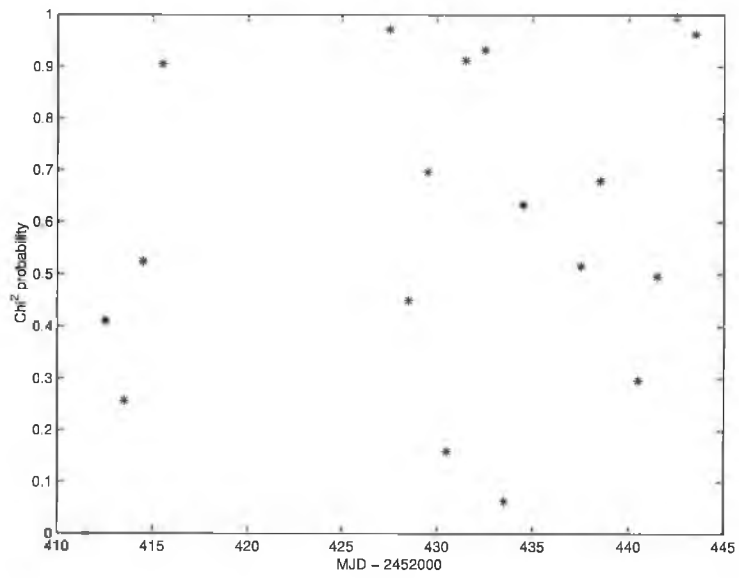


Figure 5.7: A plot of χ^2 probabilities for observing days during May and June 2002.

Chapter 6

Conclusions and Future Work

6.1 The CCD Camera and FIR Pyrometer

The SBIG ST-237 CCD camera and the Heitronics KT15.82D FIR pyrometer, installed and tested on the Whipple ten metre telescope in Arizona, have been shown to do an excellent job in performing their respective tasks.

The results from the CCD camera show that, with the $f/0.85$ lens, it can detect stars down to 9th magnitude or fainter with exposure times of 10 seconds. This lens also allows the camera to take images over a wide field of view (approximately 10.7° horizontally by 8° vertically). The CCD chip in the camera has 640×480 pixels and the angle per pixel is very close to $1'$.

The results from the FIR pyrometer show that it is very effective at detecting clouds in the field of view or general haze in the atmosphere, both of which influence the quality of the Cherenkov data detected by the telescope. The raw rate of the cosmic-ray data detected by the telescope can be used as a measure of weather conditions; however, this has the inherent disadvantage of depending on the telescope performance. The FIR pyrometer readings are shown to follow similar trends to the cosmic-ray rate; when the cosmic-ray rate falls due to deteriorating weather conditions, the FIR temperature rises due to the haze or cloud in the field of view. The pyrometer has the advantage of not depending on the performance of the telescope and also gives a more

accurate and quantifiable readout.

Currently, the CCD camera and FIR pyrometer communicate data via XML messages sent using TCP/IP. The VERITAS Collaboration made a collective decision to change all communications software to the CORBA communications package. Any future development on the CCD camera and FIR pyrometer will therefore involve a transition from XML communications to CORBA. Due to the object-oriented design of this project, the CORBA communications package can be developed and integrated without changing the driver or GUI software associated with each device.

Using the Qt and Qwt GUI packages, complicated yet user-friendly GUIs have been developed for both the CCD camera and the FIR pyrometer. The object-oriented design of these GUIs means they can be easily modified and updated as new functionality is required with future developments of the VERITAS weather monitoring project.

Future development with regard to the CCD camera and the FIR pyrometer might involve a more exact calibration of the data obtained from the devices. Images of star fields captured with the CCD camera agree well with star charts generated by *Xephem* and *Kstars*. The brightness of star images in the CCD frames has been shown to reflect closely the catalogued values of stellar magnitude. This paves the way for future development; a custom star chart program could be written, which might query the telescope's tracking computer to determine the current pointing direction. The actual magnitudes of the stars in the field of view could then be compared with those reported by the CCD camera and an assessment of the current weather conditions could be made. The current CCD software also determines the positions of the stars in the images. The telescope tracking computer could be queried to determine the telescope's nominal pointing direction. The location of the star images in the CCD frame could then be compared with the expected positions, allowing any offset in the pointing to be determined. Moreover, analysis of the widths of the star images could yield information on the short-term stability of the tracking.

A more complete study of the FIR pyrometer temperature data will prove useful for determining the weather conditions in the telescope's field of view. There are many things which affect the temperature read out from the pyrometer - the emissivity of the object(s) it is looking at and the emissivity setting used by the pyrometer; the ambient temperature at ground level and the ambient temperature setting used by the pyrometer; the integration time used by the pyrometer; and the elevation of observations. Detailed investigation of the effects of these factors will help to make the FIR pyrometer measurements even more useful in providing observers with a reliable assessment of sky clarity in the field of view of the telescope.

6.2 Active Galactic Nuclei at TeV Energies

The detection of 1ES1959+650 adds another member to the class of TeV blazars. The flux variability and the fact that this source has not been detected during previous observations indicates that it was in an unusual state of flaring during the period of observations on it in May and June 2002. Further observations at the Whipple Observatory on 1ES1959+650 will reveal more about the source's behaviour and characteristics, including the determination of its spectrum. Original attempts to reconstruct the spectrum were hampered due atmospheric pollution at the times of observation. Continued observation of 1ES1959+650 and of other known TeV blazars, both at TeV energies and in other wavelength ranges, will be of immense importance in elucidating the processes at work in these extreme environments.

1ES1959+650 is a low-redshift X-ray selected BL Lac, following the characteristics of previously detected TeV blazars. This suggests that low-redshift X-ray selected BL Lacs may be the only extragalactic gamma-ray sources observable at TeV energies. Further study of the variabilities of these objects will contribute to the understanding of acceleration mechanisms of particles in AGN. Currently, no model for the production of gamma rays in AGN is generally accepted. The two most popular models are those in which

high-energy electrons (known to be present from radio, optical and X-ray observations) produce the gamma rays by inverse Compton scattering of low energy photons and those in which very high energy (VHE) protons produce the gamma rays by initiating cascades within the jets.

6.3 The Future of Gamma-Ray Astronomy

The Imaging Atmospheric Cherenkov Technique (IACT) continues to be the favoured method of detecting gamma rays in the 100GeV–10TeV energy range. Next-generation experiments using arrays of ground-based imaging telescopes, such as the proposed VERITAS array in Arizona and the HESS (High Energy Stereoscopic System) array, proposed by the HEGRA group at the Max-Planck Institut für Kernphysik in Germany, will reduce the energy threshold for detections and help to bridge the flux-sensitivity gap between ground-based and space-borne detectors.

The next major satellite experiment, scheduled for launch in 2006, will be GLAST (Gamma-ray Large Area Space Telescope). It follows in the footsteps of the EGRET experiment, which was operational between 1991 and 1999, but is designed to operate in the energy range from 10MeV to greater than 100MeV and offers a better angular resolution, sensitivity and field of view than EGRET.

The EGRET catalogue includes in excess of 66 blazars above 100MeV (Hartman et al. 1999) and these span over a wide range of redshifts. However, only six AGN have been detected above 300GeV, all at relatively low redshifts. This is most likely due to cutoffs in source spectra and for more distant sources, attenuation of TeV gamma rays by pair production with background infrared radiation. The low-energy threshold and good sensitivity of VERITAS will help to overcome these hurdles, and can be expected to lead to discovery VHE gamma-ray emission from many new sources. The large effective area of VERITAS will enable the accurate measurement of extremely rapid variations in gamma-ray flux. Its flux sensitivity will permit

the detection of weaker sources of VHE emission and its sensitivity at lower energies will allow the viewing of objects further from the Earth and objects whose spectral cutoffs are below the sensitive range of existing Cherenkov telescopes.

With the advent of next-generation telescopes, the need to be aware of weather conditions during observations becomes increasingly important. The CCD camera and FIR pyrometer systems presented in this thesis have been shown to do an excellent job in performing this task. A CCD camera and an FIR pyrometer will be a standard adjunct to each VERITAS telescope and weather data will be integrated with the Cherenkov data files recorded during observations. Both devices provide a means of assessing the sky clarity and thereby give an objective method of judging the quality of data recorded by the gamma-ray telescope system. This provides an independent method of selecting valid Cherenkov data, with consequences for the overall gamma-ray detection efficiency. This may be crucial in the detection of weak sources and in the determination of spectral characteristics close to the trigger threshold of the telescope system.

Appendix A

Definition of the Hillas Parameters

Suppose the i^{th} PMT is given coordinates x_i, y_i (in degrees) and registers a signal s_i . The origin of the coordinate system is in the centre of the array of PMTs. An ellipse is fitted to the image and the Hillas parameters are calculated relative to the centre. Most of these parameters are illustrated in Figure 4.4. The fitting of the ellipse employs the following simple moments:

$$\begin{aligned}\langle x \rangle &= \frac{\sum s_i x_i}{\sum s_i}, & \langle y \rangle &= \frac{\sum s_i y_i}{\sum s_i}, \\ \langle x^2 \rangle &= \frac{\sum s_i x_i^2}{\sum s_i}, & \langle y^2 \rangle &= \frac{\sum s_i y_i^2}{\sum s_i}, \\ \langle xy \rangle &= \frac{\sum s_i x_i y_i}{\sum s_i}, & \langle x^3 \rangle &= \frac{\sum s_i x_i^3}{\sum s_i}, \\ \langle y^3 \rangle &= \frac{\sum s_i y_i^3}{\sum s_i}, & \langle x^2 y \rangle &= \frac{\sum s_i x_i^2 y_i}{\sum s_i}, \\ \langle xy^2 \rangle &= \frac{\sum s_i x_i y_i^2}{\sum s_i},\end{aligned}$$

and

$$\begin{aligned}\sigma_{x^2} &= \langle x^2 \rangle - \langle x \rangle^2, \\ \sigma_{y^2} &= \langle y^2 \rangle - \langle y \rangle^2, \\ \sigma_{xy} &= \langle xy \rangle - \langle x \rangle \langle y \rangle, \\ \sigma_{x^3} &= \langle x^3 \rangle - 3\langle x \rangle \langle x^2 \rangle + 2\langle x \rangle^3, \\ \sigma_{y^3} &= \langle y^3 \rangle - 3\langle y \rangle^2 \langle y \rangle + 2\langle y \rangle^3, \\ \sigma_{x^2y} &= \langle x^2y \rangle - 2\langle xy \rangle \langle x \rangle + 2\langle x \rangle^2 \langle y \rangle - \langle x^2 \rangle \langle y \rangle, \\ \sigma_{xy^2} &= \langle xy^2 \rangle - 2\langle xy \rangle \langle y \rangle + 2\langle x \rangle \langle y \rangle^2 - \langle x \rangle \langle y^2 \rangle.\end{aligned}$$

Given the following definitions:

$$\begin{aligned}k &= \sigma_{y^2} - \sigma_{x^2}, \\ l &= \sqrt{k^2 + 4\sigma_{xy}^2}, \\ m &= \langle y^2 \rangle - \langle x^2 \rangle, \\ n &= \sqrt{m^2 + 4\langle xy \rangle^2}, \\ u &= 1 + \frac{k}{l}, \\ v &= 2 - u,\end{aligned}$$

the Hillas parameters are calculated from:

$$\begin{aligned}
\langle Size \rangle &= \sum s_i, \\
\langle Length \rangle^2 &= \frac{\sigma_x^2 + \sigma_y^2 + l}{2}, \\
\langle Width \rangle^2 &= \frac{\sigma_x^2 + \sigma_y^2 - l}{2}, \\
\langle Miss \rangle^2 &= \frac{u\langle x \rangle^2 + v\langle y \rangle^2}{2} - \frac{2\langle xy \rangle \sigma_{xy}}{l}, \\
\langle Distance \rangle^2 &= \langle x \rangle^2 + \langle y \rangle^2, \\
\langle Alpha \rangle &= \sin^{-1} \left(\frac{\langle Miss \rangle}{\langle Distance \rangle} \right), \\
\langle Azwidth \rangle^2 &= \frac{\langle x^2 \rangle + \langle y^2 \rangle - n}{2}.
\end{aligned}$$

The calculation of the parameter *Asymmetry* requires the angle, ψ , between the x -axis and the major axis of the ellipse. It is convenient to define p :

$$\begin{aligned}
\psi &= \tan^{-1} \left(\frac{(k+l)\langle y \rangle + 2\sigma_{xy}\langle x \rangle}{2\sigma_{xy}\langle y \rangle - (k-l)\langle x \rangle} \right), \\
p &= \sigma_x^3 \cos^3 \psi + 3\sigma_{x^2y} \sin \psi \cos^2 \psi + 3\sigma_{xy^2} \cos \psi \sin^2 \psi \\
&\quad + \sigma_y^3 \sin^3 \psi, \\
\langle Asymmetry \rangle^3 &= \frac{p}{\langle Length \rangle}.
\end{aligned}$$

Bibliography

- Abu-Zayyad, T. et al. 1997, Proc. 25th ICRC, Durban, 5, 345
- Aharonian, F. et al. 2002, A & A, 384, L23
- Aharonian, F. A. 2000, New Astronomy, 5, 377
- Allen, C. W. 1979, Astrophysical Quantities, 3rd edn., The Athlone Press, London
- Beckmann, V. 2002, A & A, 383, 410
- Bird, D. J. 1997, Proc. 25th ICRC, Durban, 5, 353
- Blandford, R. D. & Rees, M. J. 1978, Pittsburgh Conference on BL Lac Objects, ed. A. N. Wolfe, University of Pittsburgh Press, 328
- Boella, G. et al. 1997, A & A, 122, 299
- Bradbury, S. M. 1997, Proc. International Workshop: Towards a Major Cherenkov Detector V, Kruger Park, 365
- Buckley, D. J. et al. 1999, Exp. Astron., 9, 237
- Buckley, J. H. et al. 1997, Proc. 4th Compton Symposium (AIP Conf. Proc. 410), 1381
- Catanese, M. & the Whipple Collaboration. 1999, BL Lac Phenomenon (ASP Conf. Series 159), 243

- Catanese, M. et al. 1997a, Proc. 4th Compton Symposium (AIP Conf. Proc. 410), 1376
- . 1997b, ApJ, 487, L143
- . 1998, ApJ, 501, 616
- Cawley, M. F. 1993, Proc. International Workshop: Towards a Major Atmospheric Cherenkov Detector II, Calgary, 176
- Cawley, M. F. et al. 1990, Exp. Astron., 1, 173
- Chadwick, P. M. et al. 1999, Astroparticle Physics, 11, 145
- Cherenkov, P. A. 1934, Dokl. Akad. Nauk SSSR, 2, 451
- Chevalley, P. 2001, www.cartesduciel.com
- Costamante, L. & Ghisellini, G. 2002, A&A, 384, 56C
- Davies, J. M. & Cotton, E. S. 1957, Journal of Solar Energy, 1, 16
- Dietel, H. M. et al. 2001, XML How To Program (Prentice Hall)
- Dowdall, C., Moriarty, P., & Kosack, K. 2002, IAU Circular No. 7903
- Downey, E. C. 2002, <http://www.xephem.com>
- Fegan, D. J. et al. 1983, Nucl. Inst. Meth., 211, 179
- Finley, J. P. 2001, Proc. 27th ICRC, 2827
- Gaidos, J. A. et al. 1996, Nature, 383, 319
- Harris, J., Evermann, H., Kabelmann, T., Hollomon, M., & de Vicente, P. 2001, <http://edu.kde.org/kstars>
- Hartman, R. C. et al. 1999, ApJS, 123, 79
- Hillas, A. M. 1985, Proc. 19th ICRC, 3, 445

- Holder, J., Bond, I. H., Boyle, P. J., Bradbury, S. M., Buckley, J. H., Carter-Lewis, D. A., Cui, W., Dowdall, C., et al. 2003, *ApJ*, 583, L9
- Horan, D. et al. 2002, *ApJ*, 571, 753
- Horns, D. & Konopelko, A. 2002, IAU Circular No. 7909
- Kataoka, J. et al. 1999, *ApJ*, 514, 138
- Kerrick, A. D. et al. 1995, *ApJ*, 452, 588
- Kertzman, M. P. & Sembroski, G. H. 1994, *Nucl. Inst. Meth.*, 343, 629
- Konopelko, A. 1999, *Astroparticle Physics*, 11, 263
- . 2002, *HEAD*, B17 95, 40
- Krennrich, F. et al. 1998, *Astroparticle Physics*, 8, 213
- Mannheim, K. 1993, *A & A*, 269, 67
- Maraschi, L. et al. 1999, *ApJ*, 526, L81
- Moriarty, P. et al. 1997, *Astroparticle Physics*, 7, 315
- Mücke, A. & Protheroe, R. J. 2001, *Astroparticle Physics*, 15, 121
- Mukherjee, R. et al. 1997, *ApJ*, 490, 116
- Nishiyama, T. et al. 1999, *Proc. 26th ICRC, Salt Lake City*, 3, 370
- Ong, R. A. 1998, *Physics Reports*, 305, 93
- Padovani, P. & Giommi, P. 1995, *ApJ*, 444, 567
- Pian, E. 1998, *ApJ*, 492, L17
- Punch, M. et al. 1991, *Proc. 22nd ICRC, Dublin*, 1, 464
- . 1992, *Nature*, 358, 477

- Quinn, J. et al. 1996, ApJ, 456, L83
- . 1999, ApJ, 518, 693
- Reynolds, P. T. et al. 1993, ApJ, 404, 206
- Santa Barbara Instrument Group. 1999, Operating Manual for the ST-237
Advanced CCD Camera
- Stecker, F. W., De Jager, O. C., & Salamon, M. H. 1996, ApJ, 75, 473
- Thompson, D. J. et al. 1995, ApJ Supp., 101, 259
- Urry, C. M. & Padovani, P. 1995, PASP, 107, 803
- Weekes, T. C. 1972, ApJ, 174, 165
- . 1988, Physics Reports, 160, 5
- . 1999, GeV–TeV Gamma Ray Astrophysics Workshop, Snowbird, Utah
(AIP Conf. Proc. 515), 3
- Weekes, T. C. et al. 2002, Astroparticle Physics, 17, 221